The Pennsylvania State University

The Graduate School

AN INVESTIGATION OF PARAMAGNETIC RECOMBINATION CENTERS IN 4H-SIC PIN DIODES VIA ELECTRICALLY DETECTED MAGNETIC RESONANCE

A Thesis in

Engineering Science and Mechanics

by

Ashton Purcell

© 2023 Ashton Purcell

Submitted in Partial Fulfillment
of the Requirements
for the Degree of

Master of Science

May 2023

The thesis of Ashton Purcell was reviewed and approved by the following:

Patrick M. Lenahan
Distinguished Professor of Engineering Science and Mechanics
Thesis Advisor

Saptarshi U. Das
Associate Professor of Engineering Science and Mechanics

Sahin K. Ozdemir
Professor of Engineering Science and Mechanics

Albert E. Segall
Professor of Engineering Science and Mechanics
Head of the Department or Chair of the Graduate Program

ABSTRACT

The 4H-SiC polytype is arguably the most technologically relevant due to its relatively large band-gap which give rise to its preferred application in high-power and high-temperature applications. One such application is their incorporation into pin diodes, which are used for high-power radio-frequency and microwave applications. However, little is known about the role of electrically-active defect centers in 4H-SiC pin diodes. In this work, I present an electrically detected magnetic resonance (EDMR) investigation into the physical and chemical identity of defect centers in 4H-SiC pin diodes. The EDMR spectra consisted of several overlapping defect centers whose relative amplitude vary with bias and doping concentration. These indicated the presence of multiple recombination centers with different energy levels in the 4H-SiC bandgap. Identification attempts were made by comparing experimental data with literature values. The identification of these centers and their role on pin diode device performance are crucial in improving their performance and utility.

NON-TECHNICAL ABSTRACT

Silicon carbide (SiC), more specifically, 4H-SiC has received increasing attention over the last two decades as a possible replacement to silicon as the material of choice for nano-scale electronics. For this to occur, the manufacturing of 4H-SiC must be improved to increase the quality of the 4H-SiC wafers produced. We aid in this pursuit by conducting a variety of magnetic resonance experiments on 4H-SiC pin diodes to identify these performance-limiting defects.

TABLE OF CONTENTS

LIST OF FIGURES v

LIST OF TABLES vi

ACKNOWLEDGEMENTS vii

Chapter 1 Introduction 10

- 1.1 4H-SiC 10
- 1.2 The pin Diode 14
- 1.3.1 Spectroscopic Techniques 17
- 1.3.2 Electrically Detected Magnetic Resonance 25
- 1.4 Intrinsic Defects 28
  - 1.4.1 Vacancies in 4H-SiC 29
    - 1.4.1.1 Silicon Vacancy, V_{Si} 29
    - 1.4.1.2 Carbon Vacancy, V_C 31
- 1.5 Deposition Methods 34

Chapter 2 Experimental Methods 35

- 2.1 Devices 36
- 2.2 EDMR Spectrometer 37

Chapter 3 Results 38

Chapter 4 Discussion 46

Chapter 5 Conclusion 51

References 53

LIST OF FIGURES

Figure **1-1**: Hexagonal unit cells of 4H-SiC showing a) crystal structure and lattice parameters [6] and b) crystal faces [46]. 11

Figure **1-2**: Side view of vertical pin diode structure........ 15

Figure **1-3**: The Zeeman splitting of an unpaired electron in the presence of a magnetic field. 20

Figure **1-4**: Additional splitting of the electron spin state energy levels from hyperfine interactions with S=1/2 and I=1. 23

Figure **1-5**: Simplified illustration of the local atomic environment of the silicon monovacancy. 24

Figure **1-6**: SRH model of recombination........ 26

Figure **1-7**: Atomic structure of V_C^- (*h*) and V_C^+(*k*). The percentages represent the unpaired electron's distribution density. Both defects are said to have C_{1h} symmetry as this is the true defect symmetry at very low temperatures (<50 K) which thermally averages to C_{3v} at elevated temperatures.. 32

Figure **2-1**: Typical set up of a homemade EDMR spectrometer in our lab. Devices are glued to a tee which is wired to the preamplifier for biasing. A biasing circuit was not necessary for my devices as only one value of voltage was used at a time, i.e. these are not gated devices. The tee is placed into the microwave cavity (gold) which is situated between homemade electromagnets.An audio amplifier receives a modulation signal from the computer and amplifies the output to modulation coils in close proximity to the cavity. The gaussmeter and hall probe record the value of magnetic field output by the coils. The microwave source provides the RF signal necessary to induce resonance... 37

Figure **3-1**: Two orthogonal orientations of the same pin diode forward biased at 2.20 V. The slight difference in the center crossing field between the spectra is accounted for in the resonant frequencies of the respective experiments to give an isotropic g=2.0030±0.0003.. 38

Figure **3-2**: High (red) and low (blue) forward bias SDR responses of a pin diode with its crystalline c-axis oriented parallel to B_0. A portion of the AF1 signal is distinctly separated from the majority of the response. The emergence of the AF1 signal significantly increases the g of the overall response.. 39

Figure **3-3**: Rotation of the pin diode in B0 from the parallel to perpendicular orientation. The shape and width of the response changes appreciably. The width of the perpendicular response is ~0.5 mT wider than that of the parallel response.. 40

Figure **3-4**: The change in device current at resonance as a function of forward bias…..........41

Figure **3-5**: EDMR response of pin diode with 2.6 V applied forward bias oriented parallel to B_0. The spectrum is nearly evenly dominated by the AF1 and V_{Si}^-.. 42

Figure **3-6**: EDMR response of p-well diode forward biased at 2.20 V with the c-axis parallel to B0..…..43

Figure **3-7**: EDMR response of p-well diode forward biased at 2.40 V with the c-axis parallel to B0..…..44

Figure **3-8**: EDMR response of p-well diode forward biased at 2.60 V with the c-axis parallel to B_0...45

LIST OF TABLES

Table **1-1**: Electrical Properties of SiC Polytypes and Si. 13

Table **1-2**: Experimental *g*-values and hyperfine parameters for V_{Si}^{-} in 3C-, 4H-, and 6H-SiC...30

Table **1-3**: *g*-values and hyperfine parameters of the EI5 and EI6 defects in 4H-SiC. 31

ACKNOWLEDGEMENTS

First and foremost, thank you Dr. Lenahan for making all of this possible. I'd also like to thank all of the professor's I've had along the way and the staff of the Engineering Science and Mechanics department at Penn State. To Fedor, Jim, Steve, and the rest of the boys from 101 EES, thanks for all of the great memories and for your continued guidance. There are too many names to thank everyone individually, but I deeply appreciate all of the support I've received from my friends and loved ones. Last, but certainly not least, thank you to my beloved dog and amateur spectroscopist, Echo.

This work was supported by the US Army Research Laboratory and also supported by the Air Force Office of Scientific Research under Award No. FA9550-17-1-0242. Any opinions, findings, conclusions, or other recommendations expressed herein are those of the authors and do not necessarily reflect the views of the US Army Research Laboratory or the Air Force Office of Scientific Research. This project was also sponsored by the Department of Defense, Defense Threat Reduction Agency under grant number HDTRA1-18-0012. The content of the information does not necessarily reflect the position or the policy of the federal government, and no official endorsement should be inferred.

Chapter 1

Introduction

Modern civilization is entirely dependent on electrical energy. A continuously growing global population means an increase in consumed electricity. It is estimated that global energy consumption will increase by 48% between 2012 and 2040 [1]. In general, electricity is not used directly where it is produced; it must be managed on the way to its destination via power electronics such as diodes, thyristors, and transistors. Power electronics must be able to handle extremely high electric fields, temperatures, and switching frequencies. Additionally, electricity must be processed multiple times from source to load introducing the possibility of loss which results in a reduction in efficiency of the system. Losses that occur during conduction and switching between the power device's on- and off-state must be minimized to improve efficiency.

Silicon power devices have reached an intrinsic performance limit. Industry has instead begun heavily pursuing wide bandgap compound semiconductor devices as the next evolution of power devices. Compared to silicon, 4H-SiC has a nearly three times wider bandgap, an order of magnitude larger breakdown electric field, and roughly double the thermal conductivity; all while exhibiting only a modest reduction in electron mobility.

The goal of this thesis is to provide an attempt at identifying the defects acting as recombination centers in 4H-SiC pin diodes via electrically detected magnetic resonance (EDMR). The purpose of this venture is two-fold: 1) identifying the electrically active defects present provides the manufacturer with information which they may use to optimize future fabrication processes and 2) furthering the understanding of the nature of the unique atomic-scale defects in 4H-SiC to continue pushing the envelope of spin-physics.

1.1 4H-SiC

The 4H-SiC polytype is one of the nearly 250 polytypes of SiC, and currently the most studied polytype. As illustrated in Fig. 1.1 (a), 4H-SiC has a hexagonal unit cell with a wurtzite crystal structure, with alternating sequences of Si-C bilayers which result in an ABCB stacking sequence along the crystalline c-axis. Both the Si and C have two inequivalent locations they can occupy referred to as the quasi-cubic (k) and hexagonal (h) lattice sites. The Si-C bonds are covalent, but the difference in electronegativity localizes the electron density primarily around the C atoms [2]. Commonly used crystal faces of 4H-SiC are the (0001), $(000\bar{1})$, $(11\bar{2}0)$, and $(1\bar{1}00)$ [46]. The (0001) and $(000\bar{1})$ faces are referred to as the Si and C faces, respectively. A schematic of the hexagonal unit cell is shown in Fig. 1.1 (b).

Power electronics incorporating 4H-SiC massively outperform their Si counterparts [46]. This is largely due to their superior breakdown electric field [3], which allows devices to be made 10x thinner relative to Si devices without breaking down [4]. This translates to a reduction in overall device size and therefore a reduction in the size of the magnetic parts used in switching mode design systems such as transformers, chokes, and inductors [5]. An increased breakdown field also means the device can handle much higher voltages and conduct more current. A more robust comparison of relevant material properties of SiC polytypes and Si is provided in Table 1.

Due to its wide bandgap, high thermal conductivity, and low thermal expansion coefficient, 4H-SiC is an extremely attractive material for high temperature and high power applications for use in aircraft, automotive (particularly electric vehicles), deep oil/gas extraction, and space exploration technology. Currently, the majority of 4H-SiC power devices are limited to operating temperatures of 200°C due to device packaging constraints. This is still a major improvement over the 150°C limit for most silicon devices. In 2019, Krasnov *et al.* demonstrated

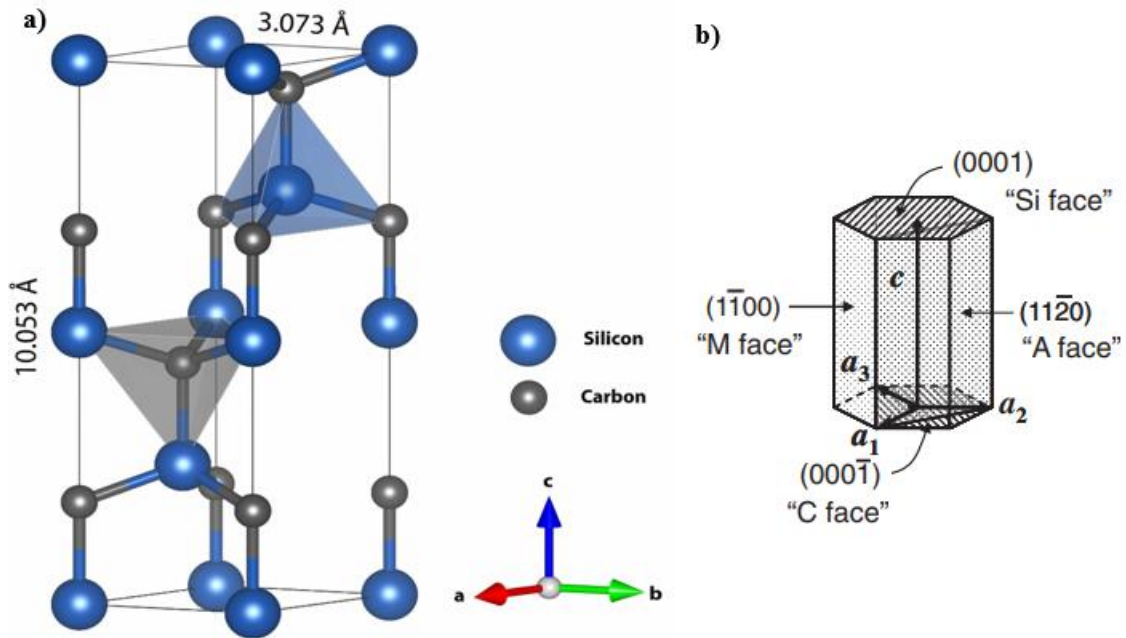

Figure 1-1: Hexagonal unit cells of 4H-SiC showing a) crystal structure and lattice parameters [6] and b) crystal faces [46].

	Si	**4H-SiC**	**6H-SiC** (⊥ c-axis)	**3C-SiC**
Bandgap (eV)	1.12	3.26	3.03	2.40
Dielectric Constant	11.9	9.70	9.66	9.72
Breakdown Field (MV/cm)	0.3	3.0	3.2	1.5
Thermal Conductivity (W/cm·K)	1.31	4.90	4.90	3.20
Intrinsic Carrier Concentration (cm^{-3})	9.65×10^9	5×10^{-9}	1.6×10^{-6}	1.5×10^{-1}
Electron/Hole Mobility ($cm^2/V \cdot s$)	1400	900	400	800
Electron Saturation Velocity (cm/s)	1×10^7	2×10^7	2×10^7	2.5×10^7

Table 1. Electrical Properties of 3C-, 4H-, 6H-SiC and Si [8, 14, 15].

a 4H-SiC Schottky barrier diode with a maximum operating temperature of nearly 1000℃ [9]. Other groups have demonstrated a range of 4H-SiC transistors with operating temperatures exceeding 400℃ [10,11,12]. Additionally, 4H-SiC has an intrinsic radiation hardness that allows for its use in deep space applications. In 2021, Gao *et al.* showed that 4H-SiC pin diodes made for excellent neutron radiation detectors, suffering almost no loss in charge collection efficiency or energy resolution [13].

Interestingly, 4H-SiC has a lower electron mobility than Si yet double the saturation velocity. In the presence of an electric field, charge carriers have a drift velocity that is proportional to their mobility. At higher fields, the velocity increases and then saturates at a maximum value. Mobility and saturation velocity are important parameters for the switching speed of transistors and diodes. In 2009, Sheng *et al*. demonstrated a 4H-SiC high-voltage lateral junction field-effect transistor capable of 3 MHz switching speeds at 200 V and 250℃. This is significantly higher than the switching speeds of similar 200 V Si devices [16].

An additional benefit of the increased breakdown field is that the intrinsic region can be doped much more heavily, due to the breakdown field having an inverse dependence with donor concentration [8]. For a given breakdown field, the doping concentration can be increased by a factor of ten while reducing the thickness by a factor of ten, resulting in a nearly two orders of magnitude reduction in forward-bias resistance [8]. This is particularly useful for power electronics where on-state resistance results in loss and decreased efficiency. The on-state resistance of a diode with an n-type epitaxial layer is expressed as [8]

$$R_{on} = \frac{V_B^2}{\mu_n \cdot \epsilon_s} \cdot \left(\frac{3}{2E_B}\right)^3, \tag{1}$$

where V_B and E_B are the breakdown voltage and field, respectively, μ_n is the electron mobility, and ϵ_s is the semiconductor dielectric constant.

In reality, these relationships are derived for unipolar devices such as Schottky barrier diodes and MOSFETs. However, pin diodes are bipolar devices. In a bipolar device, an injection of majority carriers accompanies the minority carrier injection to maintain charge neutrality. This increases the conductivity of the intrinsic region, lowering the on-state resistance even lower than what (1) predicts [8].

1.2 The pin Diode

While the pn diode is a familiar structure to most people who have taken any semiconductor physics course, the pin diode is far from mainstream. It was invented in 1952 by Jun-Ichi Nishizawa and his colleagues as a low frequency, high power rectifier [68, 69]. The key difference is the inclusion of a wide (typically 50-500μm), intrinsic region of material sandwiched between the P^+- and N^+-regions [17]. It should be noted that the intrinsic region is never truly intrinsic due to the inevitable occurrence of impurities from the device fabrication process [18, 19]. Pin diodes are typically intentionally fabricated with a lightly p-type (π) or n-type (v) intrinsic region to form the respective structures P^+-π-N^+ and P^+-v-N^+. A schematic structure of a vertical P^+-v-N^+ diode is shown in Figure 1-2. As with most SiC technology, the diodes are typically constructed vertically with the deposition of the epitaxial, nearly-intrinsic region on top of a heavily doped n^+ substrate. Although the diode is fabricated vertically, it can operate horizontally if the P^+- and N^+-regions are implanted laterally. In general, the doping concentrations of the P^+- and N^+-regions are comparable in magnitude.

For a given base width, the breakdown voltage decreases with increasing donor concentration in the i-region [19] Under reverse bias, the charge carriers are swept out of the i-region, and the diode acts as a parallel plate capacitor [4]. The reverse bias capacitance is given by [3]

$$C = \frac{\epsilon A}{W}, \quad (2)$$

where ϵ is the dielectric constant, A is the junction area, and W is the width of the i-region. The capacitance of pin diodes is typically lower than that of other diodes due to the increased plate spacing. This has the benefit of reducing RF signal loss [4].

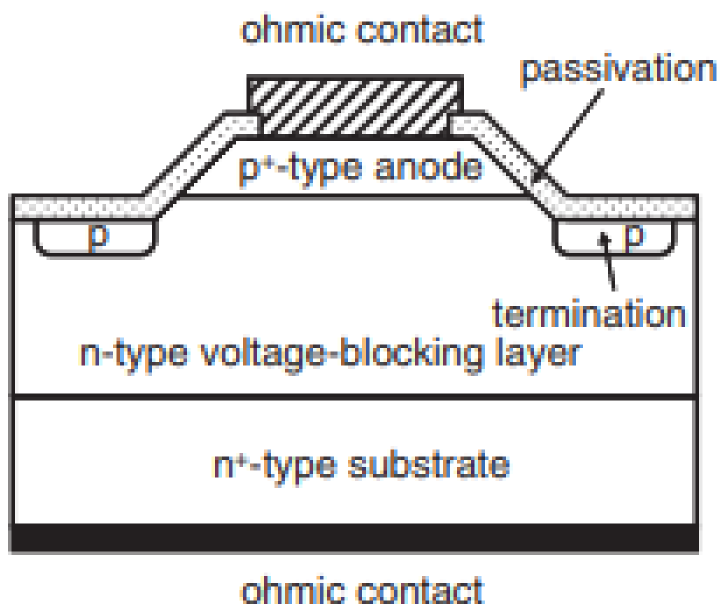

Figure 1-2: Side view of vertically fabricated and operated p^+-v-n^+ pin diode. The regions labeled "termination" are implanted to control the electric field within the diode and are typically referred to as junction termination extensions (JTEs).

Under forward bias, holes and electrons are injected into the i-region. There are two mechanisms of recombination that can occur in the i-region to facilitate current flow. The first is surface recombination which is facilitated by traps and defects that form recombination centers at the material interfaces. The second is bulk recombination, which in indirect bandgap materials, like 4H-SiC, is mostly facilitated by recombination centers

with energy levels in the bandgap. This results in a bulk recombination current that is 4 times greater than that from the end regions of the device [19].

The concentrations of holes and electrons in 4H-SiC pin diodes are highest at the P^+-i and i-N^+ interfaces, respectively. The carrier concentration across the bulk has a minimum closer to the n^+ region due to the higher mobility of electrons [7]. The resistance of the pin diode is determined from the charge density and volume of the intrinsic region [7]. When minority carriers are injected into the bulk, they have a finite lifetime before they recombine and are annihilated. This finite lifetime leads to a certain amount of stored charge in the i-region. If the device is biased to have a constant current, the stored charge is given by

$$Q = I_f \tau_{eff}, \tag{3}$$

where I_f is the forward current and τ_{eff} is the effective minority carrier lifetime in the bulk. Stored charge and forward current are then related through the first-order differential equation [18]

$$I_f = \frac{dQ}{dt} + \frac{Q}{\tau_{eff}}, \tag{4}$$

which lowers the stored charge works to lower the forward bias resistance of the i-region. This resistance can be expressed as

$$R_S = \frac{W^2}{(\mu_n + \mu_p)Q}, \tag{5}$$

where μ_n and μ_p are the mobilities of the electrons and holes, respectively [4].

One of the most notable differences between pin and pn diodes are that the depletion width of the pin diode is effectively independent of the applied bias and the electric field can be made nearly constant across it. While there are depletion regions that

occur at the junction on either side of the i-region, their contribution to the overall depletion region is so small that it is typically neglected. The electric field magnitude is zero at the outer boundary of these junction depletion regions and increases sharply to a maximum at the metallurgical junctions. The slope of the electric field is exponential away from the junction where it reaches a nearly constant value.

1.3.1 Spectroscopic Techniques

Electron paramagnetic resonance (EPR) and its related techniques have proven to be the most powerful tools in the identification of defects in semiconductor materials. EPR has the unique ability to glean atomic-scale information from any material system containing paramagnetic defect sites or sites with net spin-angular momentum [21]. In this section I will derive equations for the two most common parameters that allow for the identification of paramagnetic defects: spin-orbit coupling and hyperfine interactions. This is the first-order defect identification method; there are second and third order contributions to the equations that provide much more specificity to the defect identification.

Electrons contain two types of angular momentum: orbital- and spin-angular momentum. Orbital-angular momentum arises from the electron's orbit about the nucleus. Spin-angular momentum is classically explained as being due to the electron spinning about its own axis. However, the Dirac equation derived by Paul Dirac in 1928 led to the realization that electrons do not literally spin, and that spin-angular momentum is an intrinsic property of electrons [20]. Electrons are spin ½ Fermions meaning that

their spin-angular momentum takes the values ±1/2 along the axis of quantization (z-axis) [22]. The spin-angular momentum gives rise to an intrinsic magnetic moment of the electron given by [21,22]

$$\mu_e = -g_e \mu_B \boldsymbol{S}, \tag{6}$$

where $\boldsymbol{S} = (S_x\hat{\imath} + S_y\hat{\jmath} + S_Z\hat{z})$ is the spin quantum operator, g_e is the Landé g factor = 2.0023193043617, and μ_B is the Bohr magneton expressed as [21]

$$\mu_B = \frac{q\hbar}{2m_e}. \tag{7}$$

The negative sign in (6) is from the electron being negatively charged with the assumption that μ_B and g_e are positive.

When a magnetic dipole, such as an electron, is placed in a magnetic field, its energy is given by [21]

$$E = -\boldsymbol{\mu_e} \cdot \boldsymbol{B}. \tag{8}$$

Recalling (6), the spin-angular momentum vector, **S**, is projected along the axis of quantization and is reduced to

$$S_z = m_s. \tag{9}$$

The energy for the electron in the magnetic field becomes,

$$E = m_s g_e \mu_B B_z. \tag{10}$$

Due to $m_s = \pm\frac{1}{2}$, (10) becomes

$$E = \pm\frac{1}{2} g_e \mu_B B_z, \tag{11}$$

and the difference between the energy levels of the up and down state is given by

$$\Delta E = g_e \mu_B B_z, \tag{12}$$

which represents the splitting of a free electron's energy levels in the presence of a magnetic field. This phenomenon is often referred to as the Zeeman splitting and the simple case for an isolated unpaired electron is shown in Fig. 1-3. If microwave radiation with energy greater than or equal to (12) is applied to the system, the spin of an unpaired electron can be flipped. EPR takes advantage of this by measuring the difference in the population of the up and down spin states. The energy of a photon is given by

$$E_{ph} = hv, \tag{13}$$

where v is the frequency of the microwave radiation. Setting the difference in the magnetic field-induced splitting equal to the energy of the microwave irradiation gives us the resonance condition for the free electron

$$\Delta U = hv = g_e \mu_B B_z, \tag{14}$$

There are two conditions necessary for resonance to occur. First, the population of the low spin state must be greater than that of the high spin state [21]. At thermal equilibrium, the relative populations of the up (n^+) and down (n^-) electron spin states are given by Boltzmann's law [21,22]

$$\frac{n^+}{n^-} = e^{-\frac{\Delta E}{kT}} = e^{-\frac{g_e \mu_B B_z}{kT}}. \tag{16}$$

If this is true, the unpaired electrons in the material can exchange energy with the photons from the oscillating electromagnetic field component, B_1, of the microwave radiation. The second condition is that B_1 be applied perpendicular to B_0. Depending on the polarization of the incident photon, it will either deliver purely energy (type π), or a packet of energy and angular momentum (type σ) [22]. Multiple photons can work together to satisfy (14), but only one of type σ may be included in order to conserve angular momentum [22].

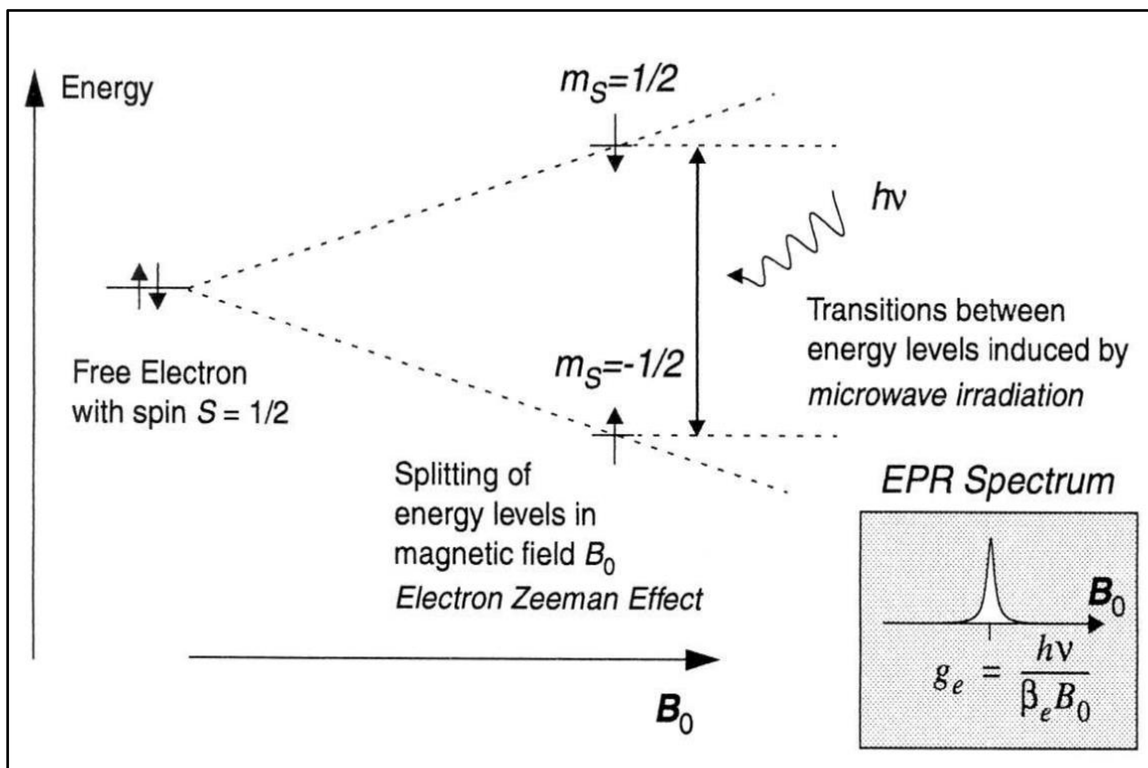

Figure 1-3: The Zeeman splitting of an unpaired electron in the presence of a magnetic field [23]. The inset shows the first-order ESR spectra for the case of a free electron placed into a magnetic field that is unperturbed by its local environment.

The analytical power of EPR, and its derivative techniques, comes from the deviations to the case of the free electron from the electron's interactions with its environment. The first deviation accounted for in the spin Hamiltonian is that due to spin-orbit coupling [21,22]

$$\mathcal{H}_z = \mu_B \boldsymbol{B} \cdot \boldsymbol{g} \cdot \boldsymbol{S}. \quad (16)$$

In (16), $\boldsymbol{g}$ is a 2nd-rank tensor [21,22]

$$\boldsymbol{g} = \begin{pmatrix} g_{xx} & g_{xy} & g_{xz} \\ g_{yx} & g_{yy} & g_{yz} \\ g_{zx} & g_{zy} & g_{zz} \end{pmatrix}. \quad (17)$$

Typically, the $\boldsymbol{g}$ -tensor is expressed in terms of the principal axis system [21,22]

$$\boldsymbol{g} = \begin{pmatrix} g_{xx} & 0 & 0 \\ 0 & g_{yy} & 0 \\ 0 & 0 & g_{zz} \end{pmatrix}. \quad (18)$$

Another deviation to the case of the unpaired electron comes from the effects of nearby magnetic nuclei near the defect electron referred to as electron-nuclear hyperfine interactions. When a nucleus has an odd number of protons or neutrons it will possess an intrinsic angular momentum that results in a magnetic moment. The interaction between the nuclear magnetic moment with the unpaired electron in a paramagnetic defect generates a local magnetic field that adds vectorially to the applied quasi-static magnetic field, $\mathbf{B_0}$. The energy levels of the electron spin states undergo an additional splitting resulting in additional lines in the spectra. The Hamiltonian for hyperfine interactions is given by [21,22]

$$\mathcal{H}_{hf} = \sum_i \boldsymbol{S} \cdot \boldsymbol{A_i} \cdot \boldsymbol{I_i}\,, \tag{19}$$

where $\boldsymbol{A_i}$ is the hyperfine coupling tensor and $\boldsymbol{I_i}$ is the nuclear spin operator of the ith nucleus. If the magnetic nuclei possesses primarily s-type orbital character, the hyperfine coupling tensor takes the form of a constant and the splitting is isotropic [21,22]

$$\boldsymbol{A_i} = A_s = \frac{2}{3}\mu_0 g_e g_N \mu_B \mu_N |\psi(0) * \psi(0)|\,, \tag{20}$$

where g_N is the nuclear g-value, μ_0 is vacuum permeability, and $|\psi(0) * \psi(0)|$ represents the electron probability density at the nucleus. If the magnetic nuclei has *p*, *d*, or *f* character, the contribution to the spin Hamiltonian for this type of electron-nuclear hyperfine interaction is given by [21,22]

$$\mathcal{H}_{dipolar}(\boldsymbol{r}) = -\frac{\mu_0}{4\pi} g_e \mu_B g_N \mu_N \left[\frac{\boldsymbol{S^T} \cdot \boldsymbol{I}}{r^3} - \frac{3(\boldsymbol{S^T} \cdot \boldsymbol{r})(\boldsymbol{I^T} \cdot \boldsymbol{r})}{r^5}\right]. \tag{21}$$

The energy of the magnetic interaction between the electron and nuclear spin is orientation dependent and varies according to r^{-3} [22]. This interaction occurs even in the absence of an externally applied magnetic field. For a p-type orbital,

the splitting will be orientation dependent, and the hyperfine interaction becomes [21,22]

$$A_p = \frac{\mu_0}{4\pi} g_e \mu_B g_N \mu_N \langle \frac{1 - 3cos\theta}{r^3} \rangle , \tag{22}$$

where the $\langle \frac{1-3cos\theta}{r^3} \rangle$ represents the time-averaged position of the electron in the orbital. It is not uncommon for hyperfine coupling to occur from interactions with orbital wavefunctions possessing a mixed character. Due to the hyperfine coupling being orientation dependent, it is often expressed as a 2nd rank tensor similarly to the ***g*** tensor. The combined Hamiltonian for spin-orbit coupling and hyperfine interactions becomes [21,22]

$$\mathcal{H} = \mu_B \boldsymbol{B} \cdot \boldsymbol{g} \cdot \boldsymbol{S} + \sum_{\boldsymbol{i}} \boldsymbol{S} \cdot \boldsymbol{A_i} \cdot \boldsymbol{I_i} \, . \tag{23}$$

Nuclei and electrons follow the same multiplicity of states based on the magnitude of their spin-angular momentum. For a nucleus with $I = 1$, there are three allowed values for its spin-angular momentum $m_I = -1,0,1$. If this nucleus were to interact with a single unpaired electron, both electron spin states ($m_s = \pm\frac{1}{2}$) would split

three times corresponding to three possible local fields for resonance to occur. This is visualized in Fig 1-4.

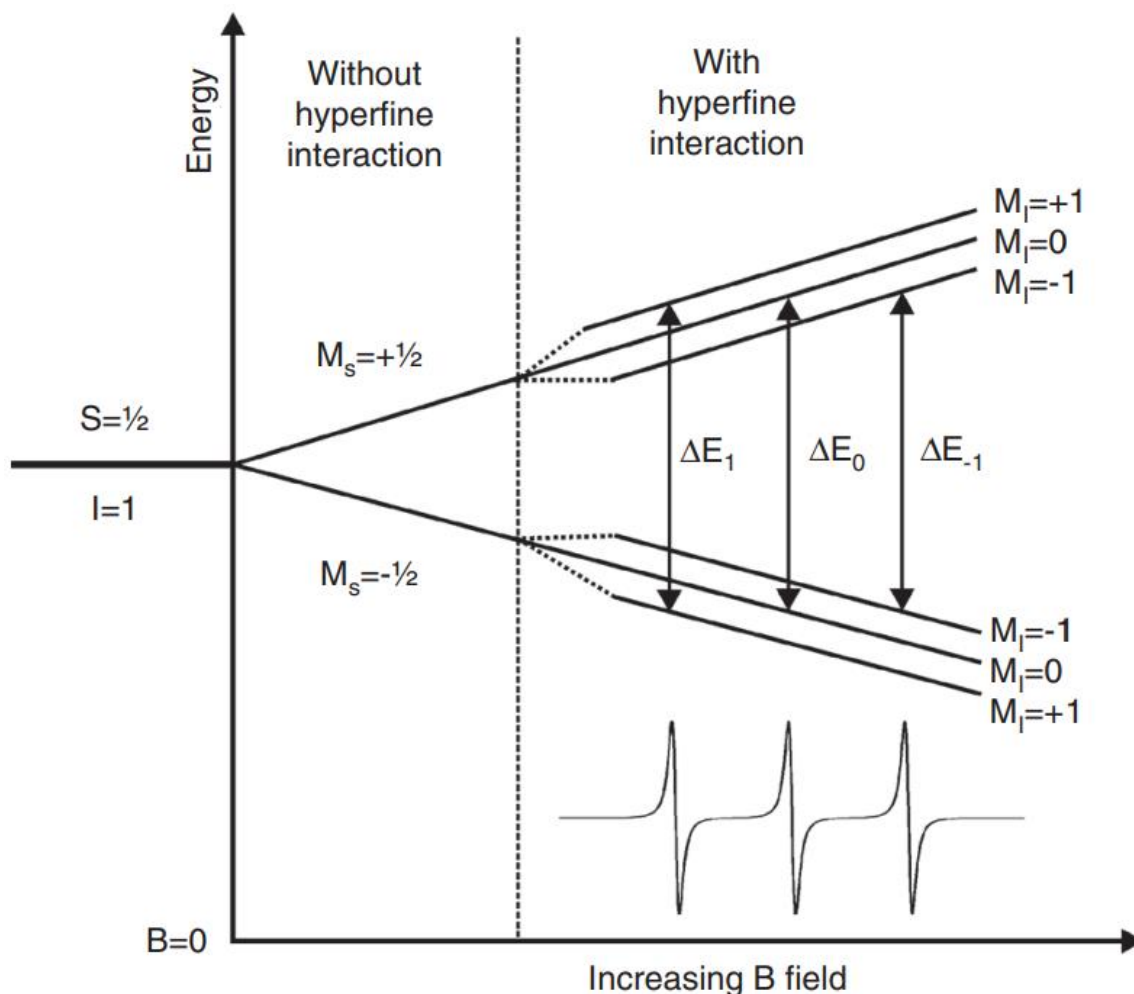

Figure 1-4: Additional splitting of the electron spin state energy levels from hyperfine interactions with S=1/2 and I=1. [24]

The relative intensity of the hyperfine lines is a function of the natural abundance of the nuclear isotope and the crystal structure of the material. In 4H-SiC, each atomic site has 4 nearest neighbors (NN) and 12 next nearest neighbors (NNN). For example, a silicon vacancy in 4H-SiC has 4 NN C atoms and 12 NNN Si atoms as shown in Fig. 1-5. Due to the magnetic interactions occurring from both Si^{29} and C^{13}, the relative integrated intensities are calculated from the product of two binomial distributions [25]

$$P(r,t) = \left[\binom{R}{r} p(Si^{29})^r \left(1 - p(Si^{29})\right)^{R-r}\right] \cdot \left[\binom{T}{t} p(C^{13})^t \left(1 - p(C^{13})\right)^{T-t}\right]. \quad (24)$$

For a silicon vacancy in 4H-SiC, R = 12 is the total number of NNN Si atoms, *r* is the number of NNN Si^{29} atoms, $p(Si^{29}) = 4.7\%$ is the natural abundance of Si^{29}, T = 4 is the total number of NN C atoms, *t* is the number of C^{13} atoms, and $p(C^{13}) = 1.1\%$ is the natural abundance of C^{13}. By modeling the intensities of the experimentally acquired spectra, the defect and its surroundings can very often be identified.

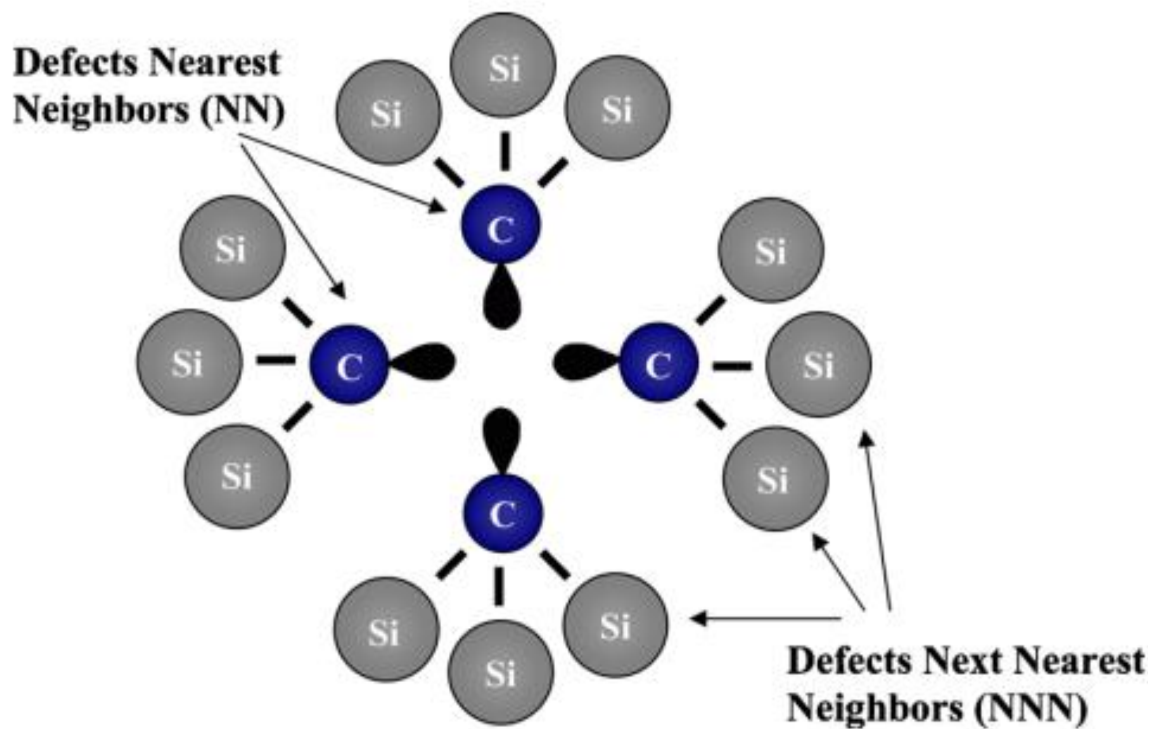

Figure 1-5: Simplified illustration of the local atomic environment of the silicon monovacancy [37].

1.3.2 Electrically Detected Magnetic Resonance (EDMR)

EDMR is a technique derived from EPR that differs in its detection scheme. In EDMR, changes in the electrical current of the device under study are monitored as the field is swept through the resonance condition. Changes in the current are due to a phenomenon called spin dependent recombination (SDR) that occurs under resonance. The total number of defects present in the device decreases as the overall size of the device is decreased. While EPR lacks the sensitivity to detect the number of defects present in modern day devices, EDMR has ten million times the sensitivity of EPR making it suitable for the job. Since EDMR measures a change in device current, it is only sensitive to those paramagnetic defects in the electrically active regions of the device.

Recombination is the process of a conduction band (CB) electron pairing with a valence band (VB) hole resulting in their annihilation and a reduction in device current. Trap-assisted recombination was explained by Shockley, Read, and Hall (SRH) in 1954 [28,29]. The SRH model of recombination through defects is described by 4 processes: electron capture, electron emission, hole capture, hole emission. Electron capture is when the CB electron drops to the defect energy level. Electron emission is when the trapped electron jumps back to the CB. Hole capture is when a VB hole jumps to the defect energy level which can alternatively be thought of as the trapped electron transitioning down to the VB. Hole emission is the process of a trapped hole dissociating from the defect and traveling back to the VB, alternatively this can be envisioned as a VB electron being excited to the defect energy level. These processes are visualized in Fig. 1-6.

A major shortcoming of the SRH model is that it does not account for spin. In 1972, Lepine proposed a relatively simple SDR model by combining the SRH model with the Pauli exclusion principle [30]. In his model he introduced a spin-dependent capture cross-section that

was a function of the applied magnetic field. However, the observed changes in current due to SDR are often approximately two to three orders of magnitude greater than his model predicted. Kaplan, Solomon, and Mott (KSM) introduced a much better model of SDR in 1978 [31]. The novel idea in their SDR model was the introduction of a spin pair. If spin-orbit interactions are relatively small, the recombination process conserves spin angular momentum. Provided the final state of the system has $S = 0$, the system must have started in an $S = 0$ configuration.

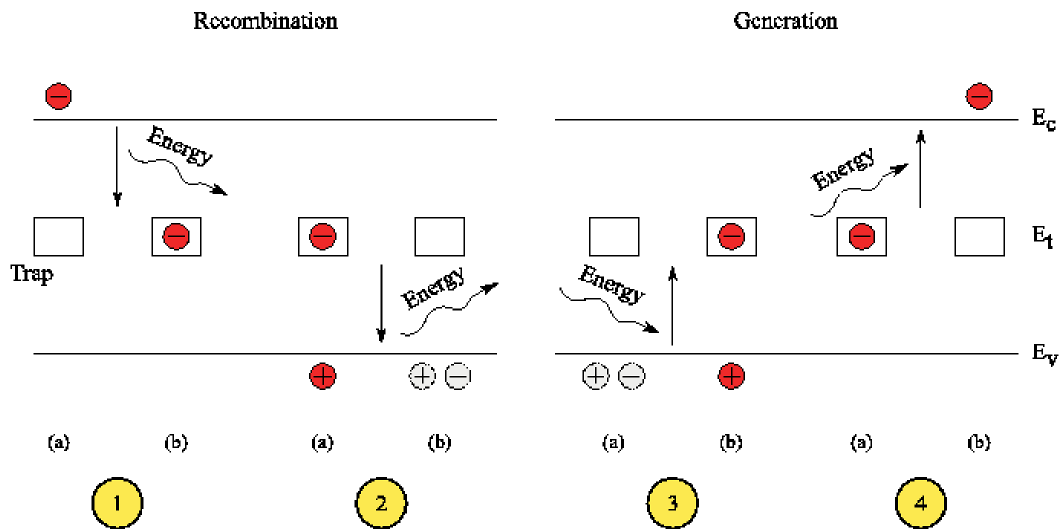

Figure 1-6: The SRH model of recombination. 1) Electron capture: The CB electron loses energy and falls to the defect energy level. 2) Hole capture: The e^- now occupying the defect loses more energy and falls to the VB where it recombines with a hole. 3) Hole emission: Despite the name it is most commonly described as a VB e^- gaining energy and jumping to the defect energy level generating an electron-hole pair (EHP). 4) Electron emission: The trapped e^- gains energy and dissociates from the defect back into the CB. Processes 3 & 4 result in an EHP and are regarded as generative, while processes 1 & 2 result in the annihilation of an EHP through recombination. [8]

This means that in order for spin-dependent capture events to occur in the recombination process, the spins must be aligned antiparallel in the singlet configuration. If the spins are aligned parallel in the triplet configuration, the CB electron will dissociate back to the CB after a finite amount of time. Thus, the overall recombination rate is dependent on the singlet recombination rate. KSM suppose that if spin pairs are generated from an isotropic distribution of charge carriers that the singlet states will have a much shorter lifetime, and thus a lower equilibrium population than the

triplet states [31]. By introducing a microwave field that saturates the electron spin resonance the isotropic spin distribution is recovered. This results in an increase in singlets and their recombination rate.

In reality, the recombination of a CB electron with a VB hole can be facilitated by multiple paramagnetic centers with energy levels in the bandgap. Electrons in the CB can form intermediate spin pairs with singly occupied paramagnetic centers whose energy level is near the CB minimum. The CB electron effectively uses this shallow paramagnetic center as a steppingstone to transition to the deep level (DL) defect whose energy is more near the middle of the bandgap. From the DL defect, the CB electron can recombine with a VB hole and contribute to the recombination current. Multiple groups have used a technique called spin-dependent charge pumping (SDCP) to illustrate this process in MOSFETs [47,48]. In SDCP, a trapezoidal voltage waveform is applied to the gate while the source-to-body diode is forward biased. The continuous trapezoidal waveform causes the channel to alternate between inversion and accumulation at the charge pumping frequency. The traps are filled by CB electrons during inversion. As the waveform begins its fall, the untrapped CB electrons are swept out and VB holes are accumulated at the interface to recombine with the trapped electrons. In 2019, Hori et al. showed that multiple paramagnetic centers with different levels in the bandgap of Si MOSFETs contributed to recombination [47]. As mentioned previously, the CB electrons can form intermediate spin pairs with defects whose energy is in the bandgap. In the SRH model, only the spin pair between the CB electron and a single deep-level defect is considered. However, Hori et al. show that paramagnetic centers with shallow energy levels (typically from dopants) can form extended intermediate spin pairs with the deep level defects [47].

In EDMR, as in EPR, the device is placed in a large, slowly varying magnetic field, B_0, that polarizes the spins of the unpaired electrons, and an EM field, B1, to induce resonance. When the resonance condition is met, the spins of each electron are able to flip their orientation and the

possibility of an allowed transition is increased. This increases the ratio of singlet to triplet states which increases the recombination rate which is reflected in the current and is what is measured in EDMR to generate the spectra. In general, resonance is much more effective at the deep-level defect, thus this is where it is most often observed [22]. Once recombination occurs, the electron-hole pair is annihilated, and the defect becomes available to facilitate another recombination event.

The three most common types of recombination are Auger, radiative, and trap-assisted. Auger recombination involves the direct recombination of the CB electron with the VB hole. This is not a radiative process so the excess energy is given off to a third charge carrier, promoting it either further into the CB if it's an electron or deeper into the VB if it's a hole [26]. Auger recombination probability is a strong function of carrier concentration; therefore, it is primarily a recombination mechanism occurring in the highly doped regions of the diode [19]. The probability of Auger recombination drops significantly as bandgap is increased. Radiative recombination is a similar process, but instead of exciting a charge carrier, a photon is emitted. The photon's energy is equal to the bandgap because energy is conserved in this process [27]. This type of recombination is typically only seen in direct bandgap semiconductors and makes them useful as light-emitting diodes (LEDs). It can occur in indirect bandgap materials like 4H-SiC if a phonon is emitted to conserve momentum [49].

1.4 Intrinsic Defects in 4H-SiC

The effects of point defects, impurities, and extended structural defects on device reliability and performance are crucial issues in the realization of reliable high power 4H-SiC devices. These material defects can occur from both the material growth and device fabrication processes. Point defects are classified into the categories of vacancies, interstitials, antisites, and

impurities with non-zero nuclear magnetic moment. The constituent atoms of SiC each have a non-zero abundance of isotopes with nuclear spin. The abundances of Si^{29} and C^{13} are 4.7% and 1.1%, respectively. The wavefunction of the defect's unpaired electron extends at least to its 4 nearest neighbors (NN) and 12 next nearest neighbors (NNN) resulting in hyperfine interactions if one of them happens to be a magnetic nucleus. There is not enough EPR/EDMR related literature on extended structural defects for me to include a section on them in this thesis. As for impurities, I discuss the primarily relevant impurity, nitrogen, in my Discussion chapter.

1.4.1 Vacancies in 4H-SiC

Due to its binary nature, there are two primary types of point defect vacancies in 4H-SiC: the silicon vacancy, V_{Si}, and the carbon vacancy, V_C. More complex vacancy defects can exist such as divacancy pairs, vacancy-interstitial pairs, and antisite-vacancy pairs. Two inequivalent lattice sites for Si and C are present in 4H-SiC and referred to as the hexagonal (*h*) and quasi-cubic (*k*) sites. Therefore, two variations of each vacancy exist with their own unique characteristics. Via DFT calculations it has been determined that the formation energy of V_{Si} is much greater than that of V_C indicating that the concentration of V_C should be orders of magnitude greater than V_{Si} [50, 51]. Multiple groups have attempted to predict the possible charge states of V_{Si} and V_C through various DFT calculations. Most groups agree on the possible charge states for V_{Si} and V_C including 0, -1, -2, and ±2, ±1, 0, respectively [32, 52]. However, Torpo et al. believe that V_{Si} can also exist in the +1, -3, and -4 charge states [50].

1.4.1.1 Silicon Vacancy, V_{Si}

Both $V_{Si}(k)$ and $V_{Si}(h)$ exhibit C_{3v} symmetry with the 4 nearest neighbor C atoms experiencing a slight outward deformation from their regular tetrahedral structure [33]. The C atoms along the c-axis in the tetrahedron around the vacant silicon are not symmetry related to the C atoms in the basal plane. So far, out of the possible charge states predicted by DFT, only V^{-}_{Si} has been conclusively identified in 4H-SiC. In 1997, Wimbauer et al. confirmed through analysis of the hyperfine splittings and electron-nuclear double resonance (ENDOR) that V^{-}_{Si} has the S=3/2 high spin configuration. The difference in Zeeman and hyperfine interactions between the inequivalent lattice sites was too small to be experimentally resolved so they were taken to be the same. In 2003, Orlinski et al performed W-band (95 GHz) EPR on neutron irradiated n-type 4H-SiC samples [53]. The higher frequency measurement allowed them to discern the slight anisotropy in the g of V^{-}_{Si} at the h and k sites. $V^{-}_{Si}(k)$ had an isotropic $g = 2.0032$, while the h site displayed a slight anisotropy of $g_{\parallel}(h) - g(k) = 0.00004$ and $g_{\perp}(h) - g(k) = 0.00002$ [53]. These values are well within the experimental error and therefore unresolvable at X-band. The g-values and hyperfine parameters are summarized in Table 2.

Table 2: Experimental g-values and hyperfine parameters for V^{1-}_{Si} in 3C-, 4H-, and 6H-SiC [33]

	g	A_{Si} (G)	$A_{C\parallel}$ (G)	$A_{C\perp}$ (G)
4H-SiC	2.0034	2.98	28.6	12.1
6H-SiC	2.0015	2.97	28.7	11.5
3C-SiC	2.0029	2.94	26.6	11.8

In 2022, Abe et al. definitively identified the negatively charged silicon vacancy at the quasi-cubic site, $V^{-}_{Si}(k)$ in 4H-SiC MOSFETs via X-band (~9.5 GHz) EDMR [34]. The $V_{Si}^{-}(k)$ in 4H-SiC is commonly referred to as the T_{V2a} defect in the literature. By utilizing the BAE biasing

scheme [35], they were able to tune the charge state of the silicon monovacancies generated in the channel region by proton irradiation. The T_{V2a} was noted to undergo the following changes in charge: (-1/0) below V_g = -3V, and (-1/-2) above V_g = +2V. The vacancy was singly charged between $-2 \leq V_g \leq +1$. Abe et al. were able to discern between the quasi-cubic (*k*) and hexagonal (*h*) vacancy sites from the presence of zero-field splitting (ZFS) in the (*k*) vacancy that is absent in the (*h*) response. The defect was found to have an isotropic $g = 2.0029$ and a zero-field splitting of 70 MHz. This defect is currently of great interest as a spin qubit for quantum sensing, communication, and computing [34].

1.4.1.2 Carbon Vacancy, V_C

In 2004, both variations of the positively charged carbon vacancy in p-type 4H-SiC were identified by Umeda et al. via X-band EPR [2]. Dubbed the EI5/EI6 defect before identification, they have been attributed to the $V_C^+(k)$ and $V_C^+(h)$ defects, respectively. Both defects are S=1/2 with C_{3v} symmetry. EI5/EI6 both show 4 HF interactions corresponding to the 4 NN Si of a carbon vacancy. However, the g-values and HF parameters for EI6 displayed a different orientation dependence and were heavily temperature dependent in contrast to that of EI5. These parameters are given in Table 3.

Table 3: g-values and hyperfine parameters of the EI5 and EI6 defects in 4H-SiC [2]

	g		**A (G)** (Si1)		**A (G)** (Si2-4)		
	$g_\parallel$	$g_\perp$	$A_\parallel$	$A_\perp$	$A_\parallel$	$A_\perp$	$\theta_\parallel$
EI5 (150 K)	2.00322	2.00484	64.90	44.70	51.80	36.30	109.2°
EI6 (293 K)	2.0032	2.0046	122.90	84.50	32.10	22.00	103.6°
(150 K)	2.00305	2.00472	130.60	89.70	29.70	20.10	102.6°
(50 K)	2.00279	2.00489	142.60	97.70	25.80	17.20	101.0°
(10 K)	2.0026	2.0052	154.80	106.10	21.10	13.90	97.7°

In 2005, Umeda et al. identified the (*h*)-site negatively charged carbon vacancy in n-type 4H-SiC via X-band EPR [36]. This was accomplished by comparison of HF parameters from EPR results with those from first-principles calculations. The n-type samples were irradiated with a 3.5 MeV e-beam to generate the V_C followed by an 850 °C anneal that pins the Fermi level above midgap which the group states is necessary for the detection of V^-_C. A multitude of new EPR centers (HEI1-HEI8) appeared in the samples. HEI1 is S=1/2 and shows two strong HF interactions whose intensity ratio corresponds to interactions with a Si^{29} NN. This strongly suggests that that the defect is a V^-_C which is confirmed by the angular dependence of the HF interactions. First-principles calculations indicate very different behavior for V^-_C at the (*h*) and (*k*) sites. The Jahn-Teller distortion at the (*h*) site causes the unpaired defect electron to localize more around Si_1 (c-axial) and Si_2 (basal plane) which contrasts with the (*k*) site where the unpaired electron is expected to localize primarily on Si_3 and Si_4 causing a marked change in the HF angular dependence of the EPR response. The defect structure can be seen from Fig. 1-7.

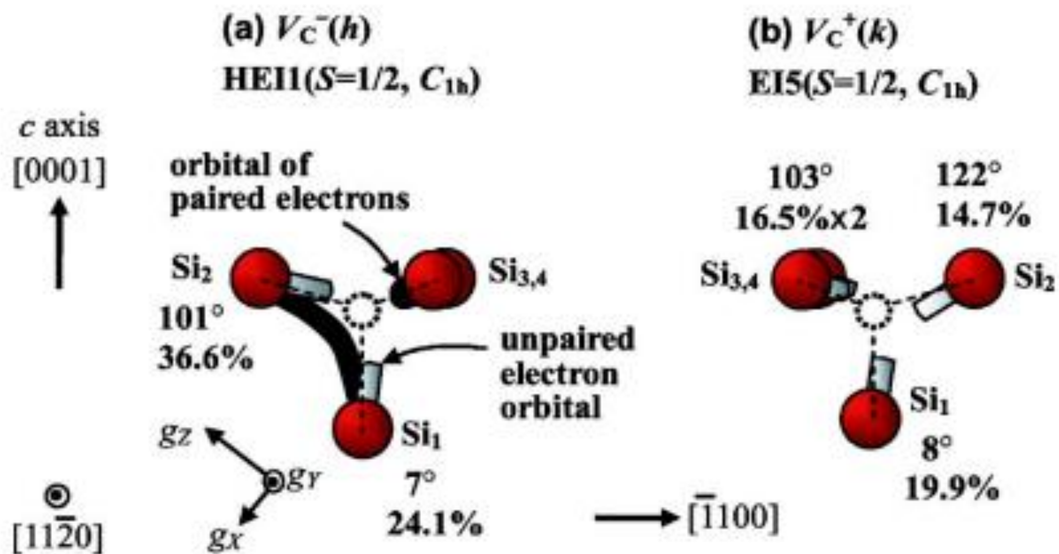

Figure 1-7: Atomic structure of V_C^-(h) and V_C^+(k). The percentages represent the unpaired electron's distribution density around the 4 NN Si atoms. Both defects are said to have C_{1h} symmetry as this is the true defect symmetry at very low temperatures (<50 K) which thermally averages to C_{3v} at elevated temperatures.[36]

Photo-EPR was performed to estimate the $V_C^-(h)$ energy level in the bandgap. Incident photons with an energy of 1.1 eV increased the EPR signal intensity by exciting electrons from defect levels just below the Fermi level to the CB. This resulted in a change in charge state for the defect from which the electron escaped to the CB. The increase in the HEI1 signal is attributed to the V^{2-}_C generating $V^-_C(h)$ when the Fermi level is located 1.1 eV below the CB.

A few years later, Son et. al [41] and Trinh et. al [43] were able to resolve both spectra for $V^-_C(h)$ and $V^-_C(k)$ as well as attribute them to the Z1 and Z2 defect centers. Z1 and Z2 are related to the more infamous minority carrier lifetime killing $Z_{1/2}$ defect in 4H-SiC [40]. Increasing our understanding of their recombination, formation, and annealing mechanisms is critical to improving device performance. Additionally, the $Z_{1/2}$ center may be of interest for quantum applications as they are color centers with long spin-coherence times [39]. Jahn-Teller distortions from the rearrangement of silicon dangling bonds leads to a lowering of symmetry from C_{3v} to C_{1h} (thermally averages to C_{3v} at higher temperatures) and to negative-*U* behavior of V_C [41,43]. This means that the V^-_C can capture a second electron so long as its binding energy is stronger than the Coulombic repulsion from the first electron [42]. EPR and Photo-EPR results show that $Z_{1/2}$ is a double acceptor state (2-|0), V_C^{2-}, and that EH_7 is a single donor state (0|+), V_C^+ [41]. At lower temperatures, V_C prefers to capture a 2nd electron to lower its energy level. This results in a non-paramagnetic S=0 spin state, therefore $Z_{1/2}$ is not directly observable via EPR [41]. $Z_{1/2}$ is the preferred stable configuration below 90K. At elevated temperatures, electrons can be thermally excited to populate the Z1/Z2 states ($V_C^-(h)$/ $V_C^-(k)$) with energy levels slightly closer the CB minimum. The defects were able to be resolved from each other due to differing electron distributions on the 4 NN Si atoms which alter the HF responses and were supported by theoretical calculations [43]. Additionally, the two defects have differing energy levels in the bandgap with Z2 being slightly lower than Z1 but still above that for $Z_{1/2}$. The population of Z1/Z2 centers is dependent on the initial concentration of $Z_{1/2}$ centers, which is

limited by the low concentration of donors in lightly doped n-type epitaxial layers. This makes detecting their presence without illumination difficult in low doped samples [43]. The $Z_{1/2}$ and EH6/7 defect concentrations have been shown to decrease from C implantation, annealing, and thermal oxidation, which further support the conclusion that they originate from V_C [44,45]. Implantation creates a source layer of C_i which can diffuse to annihilate the V_C upon annealing at 1600 °C [44]. Thermal oxidation forms a native layer of SiO_2 on the Si-face of 4H-SiC. However, there is a lattice mismatch between the materials that creates a compressive lateral strain in the 4H-SiC layers near the interface. To alleviate the strain, some C are ejected from the interface to the bulk as interstitials where they annihilate V_C.

1.5 Deposition Methods

SiC can be deposited by either physical vapor deposition (PVD) and chemical vapor deposition (CVD). The basis of PVD lies in the chemical process of sublimation where the two variables of interest are temperature and concentration of the gaseous species [38]. Powdered SiC is placed in the bottom of a graphite crucible surrounded by a high-pressure (1.5-5 kPa) atmosphere of Argon [38]. The crucible is heated in excess of 2000 °C where the powdered SiC sublimates into Si, Si_2C, and SiC_2 [38]. The gaseous compounds condense onto the crystal seed at the top of the crucible [38]. This process produces wide-diameter crystals at a relatively high growth rate of approximately 0.5-2 mm/hr [38]. Stress from the thermal gradient, polytype instability, and a noticeable defect density contribute to the disadvantages of PVD.

Chemical vapor deposition (CVD) is a method of depositing material onto a substrate via a chemical reaction taking place on the substrate surface. CVD can be carried out at various temperatures and pressures to suit different requirements of the film. The six basic steps of CVD are as follows: diffusion of vapor phase growth species to the substrate surface, adsorption of the

film precursor to the growth surface, surface diffusion of the adsorbed species, nucleation and island growth, desorption of unused reaction products, diffusion of reaction products back into the bulk gas to be pumped out.

SiC epitaxy is a step flow process which requires off-axis substrates with steps and terraces [57]. The industry standard for 4H-SiC is a 4° off-axis substrate. Growth is limited by the diffusion rate of Si to the surface (mass-transport limited). Epitaxy is also typically grown on the Si-face of the substrate [57]. Common growth parameters are temperatures around 1650 °C and pressures between 5-10 kPa. Silane (SiH_4) has been the industry standard Si source; however, silicon nucleation occurs beyond deposition rates of 10 μm/hr [57]. To overcome this, Cl is added to the gas stream allowing for deposition rates beyond 100 μm/hr [57]. Carbon is supplied to the reaction from propane (C_3H_8) or halogenated hydrocarbons (CH_xCl) [57]. The doping of the epitaxial layer is determined by the C/Si ratio [57,58]. Dopants are incorporated substitutionally in the SiC lattice with N incorporating at the C site and Al incorporating at the Si site [57,58]. If the C/Si ratio is increased, the film will be p-type, if it is decreased, the film will be n-type [58]. Hydrogen is an ingredient in both precursor gasses and is known to form complex defects.

For 4H-SiC power devices to realize their full potential in the market, thick (> 100 μm) epitaxial layers must be grown fast with high purity and long carrier lifetimes. As of 2017, the concentration of V_C, $[V_C]$, in epitaxial layers was 10^{12} cm^{-3} pre-anneal and 10^{14} cm^{-3} following a ~1900 °C anneal [45]. By slowly cooling the layers after the high temperature anneal, $[V_C]$ is drastically reduced. A cooling rate of 0.25 °C/s resulted in the highest quality epitaxial layers [45].

Chapter 2

Experimental Methods

2.1 Devices

The results presented in this thesis were collected from two differently fabricated 4H-SiC pin diodes provided by GE Research. Both diodes are fabricated on an n^+ substrate from Cree/Wolfspeed with a thick n-type epitaxial region grown on the substrate surface that is doped at a concentration of $5 \times 10^{14}\ cm^{-3}$. Heavily doped N+ and P+ regions are implanted into the n-epi with roughly equal doping concentrations of $10^{20} cm^{-3}$. The primary difference between the two types of diodes is in the "intrinsic" regions. One diode makes use of the n-epi as the nearly intrinsic region of the diode separating the highly doped N+ and P+ regions forming a N+/N-/P+ structure. This diode will be referred to as the "pin diode" because it possesses a more typical pin diode structure. The other diode has a p-type "well" (P-well) implanted into the n-epi which encapsulates both highly doped regions of the diode. This P-well is more highly doped than the n-epi with acceptors at ~$1 \times 10^{17} cm^{-3}$ and acts as the diode's nearly intrinsic region forming a N+/P/P+ structure. The intrinsic region of this diode is more highly doped than a typical pin diode and will therefore be referred to as the P-well diode. Al was used as the acceptor dopant and N was used as the donor dopant. The dopant profile of the implanted regions is strongest between 0.2 - 0.4 μm of the surface and was nearly undetectable beyond 0.6 μm. The epitaxial layer of the diodes is over 15-18 μm thick grown 4° off-axis from [0001]. Both diodes have a passivating layer of SiO_2 grown directly on the 4H-SiC epitaxial layer. Due to the horizontal operating nature of these diodes, this results in the 4H-SiC/SiO_2 interface being in direct contact with the nearly intrinsic, electrically active regions of the diodes. Interconnect metal was deposited directly on

top of the implanted N+ and P+ regions, the oxide does not appear to come between the contact and implanted regions.

2.2 EDMR Spectrometers

All of the data collected for this thesis comes from X-band EDMR spectrometers. These systems are comprised of a high current DC power supply, X-band microwave bridge, Lakeshore Cryogenics model 475 Gaussmeter and Hall probe, Stanford Research Systems SR570 low-noise current preamplifier, and custom-built electromagnets. The EDMR software and virtual lock-in amplifier were designed in LabVIEW. A computer with a National Instruments DAQ card is used to interface between the spectrometer and software. This setup is shown in Figure 2.1.

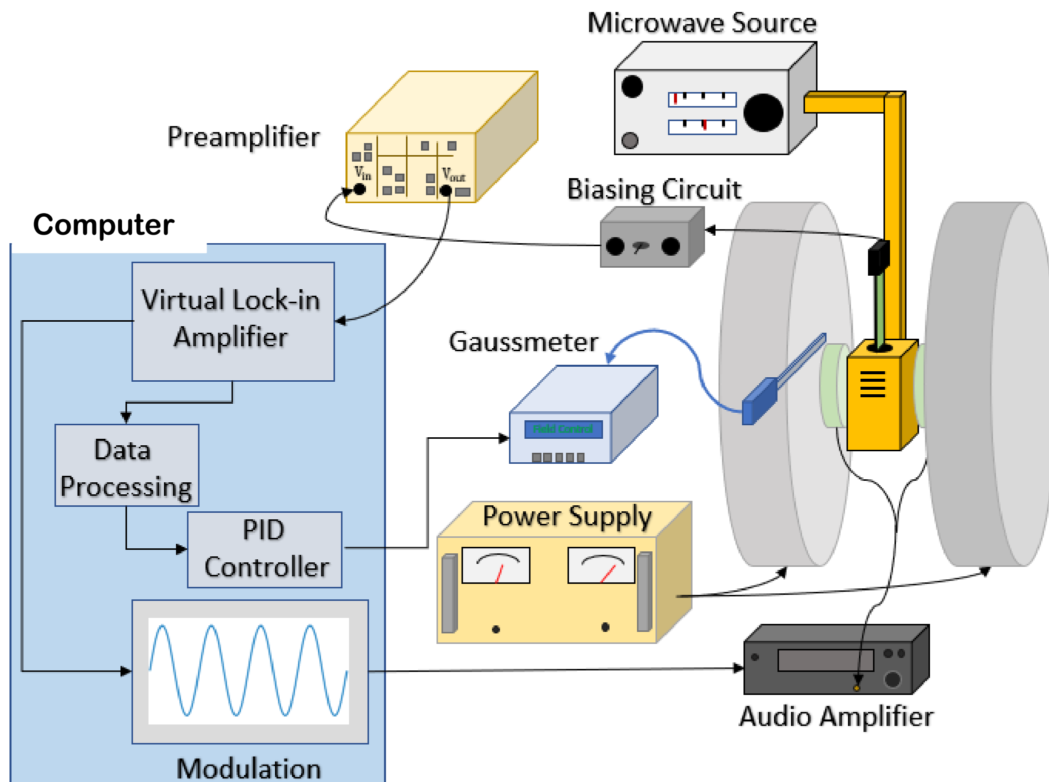

Figure 2-1: Schematic of an EDMR spectrometer [70].

In the typical set up of a homemade EDMR spectrometer in our lab, devices are glued to a tee which is wired to the preamplifier for biasing. A biasing circuit was not necessary for my devices as only one value of voltage was used at a time as these are not gated devices. The tee is placed into the microwave cavity (gold in Fig 2-1) which is situated between two homemade electromagnets. An audio amplifier receives a modulation signal from the computer and amplifies the output to modulation coils in close proximity to the cavity. The temperature compensated Hall Gaussmeter monitors the value of the magnetic field. The microwave source provides the RF signal necessary to induce resonance.

Chapter 3

Results

I present the first observations of paramagnetic recombination centers via electrically detected magnetic resonance (EDMR) in 4H-SiC pin (p-well) diodes. Upon acquiring these devices I performed a forward bias study as the first step in my attempt to elucidate and ultimately decode the SDR response of the devices. At low forward bias, the X-band EDMR

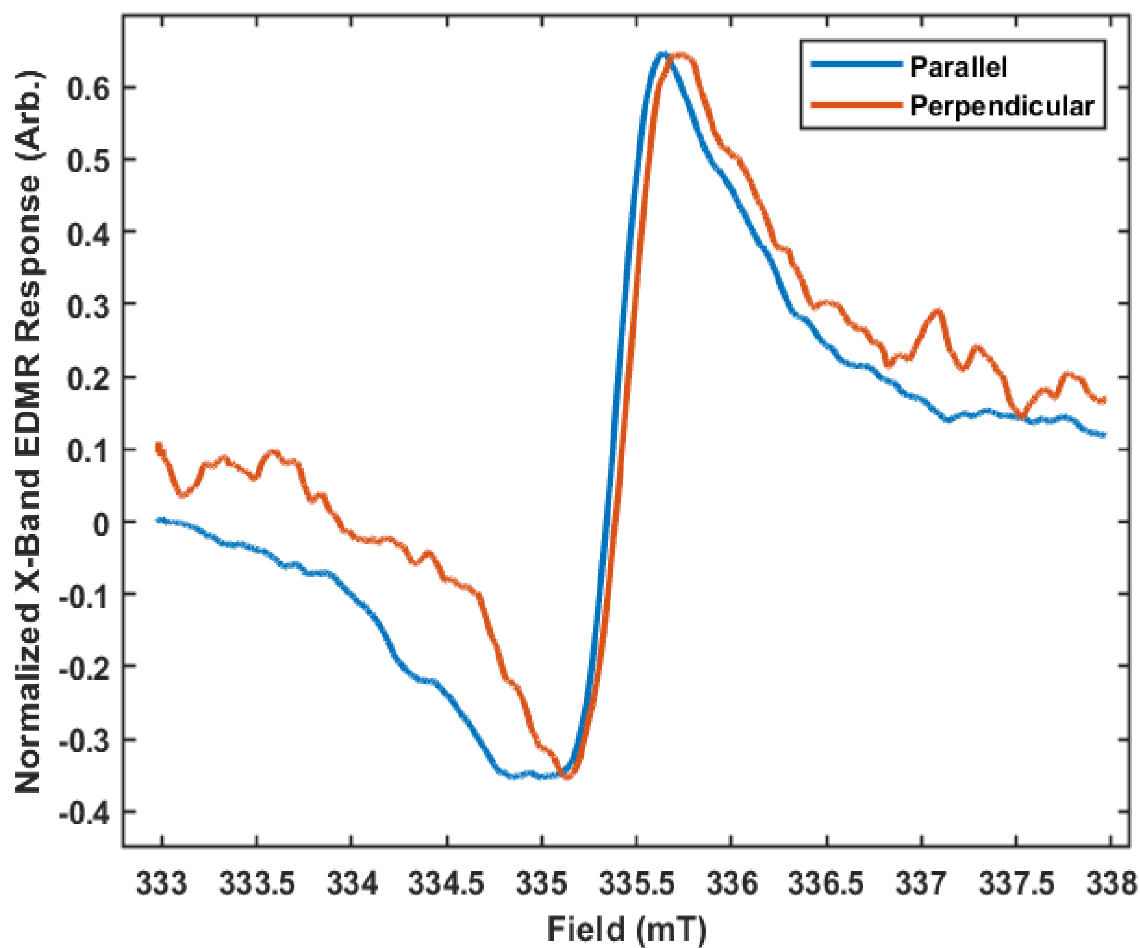

Figure 3-1: Two orthogonal orientations of the same pin diode forward biased at 2.20 V. The slight difference in the center crossing field between the spectra is accounted for in the resonant frequencies of the respective experiments to give an isotropic g=2.0030±0.0003.

response of the pin diodes is dominated by an isotropic defect with a $g = 2.0030 \pm 0.0003$ as seen in Fig 3-1.

This is most likely the V_{Si}^- defect resonance, whose experimentally reported isotropic g ranges from $g = 2.0028 - 2.0032$, it will be referred to as such for the rest of the thesis [53,55]. As forward bias is increased above 2.4-2.5V, another signal appears in the response that is highly anisotropic. I will refer to this new signal as the AF1 going forward. When the crystalline c-axis of the device is oriented parallel to the quasi-static magnetic field, B_0, a portion of the AF1 is

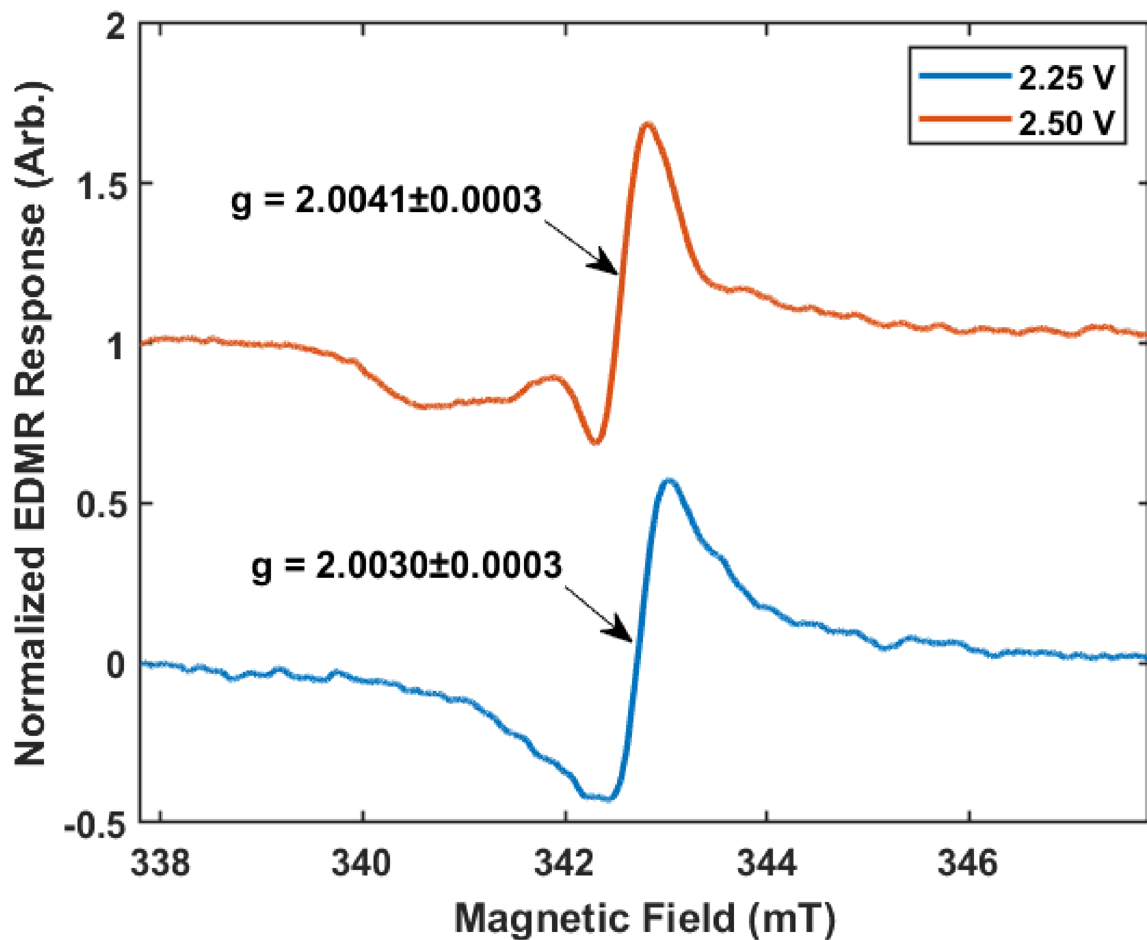

Figure 3-2: High (red) and low (blue) forward bias SDR responses of a pin diode with its crystalline c-axis oriented parallel to B_0. A portion of the AF1 signal is distinctly separated from the majority of the response. The emergence of the AF1 signal significantly increases the g of the overall response.

distinctly separated from the signal at 2.0030 and appears at a lower magnetic field (higher *g*) shown in Fig 3-2.

It is difficult to determine where the center crossing of the AF1 occurs in order to assign it a definitive *g* for this orientation. As the device is rotated so that the c-axis is perpendicular to B_0, the AF1 signal shifts position to be nearly superimposed over that of the signal at 2.0030 (Fig 3.3).

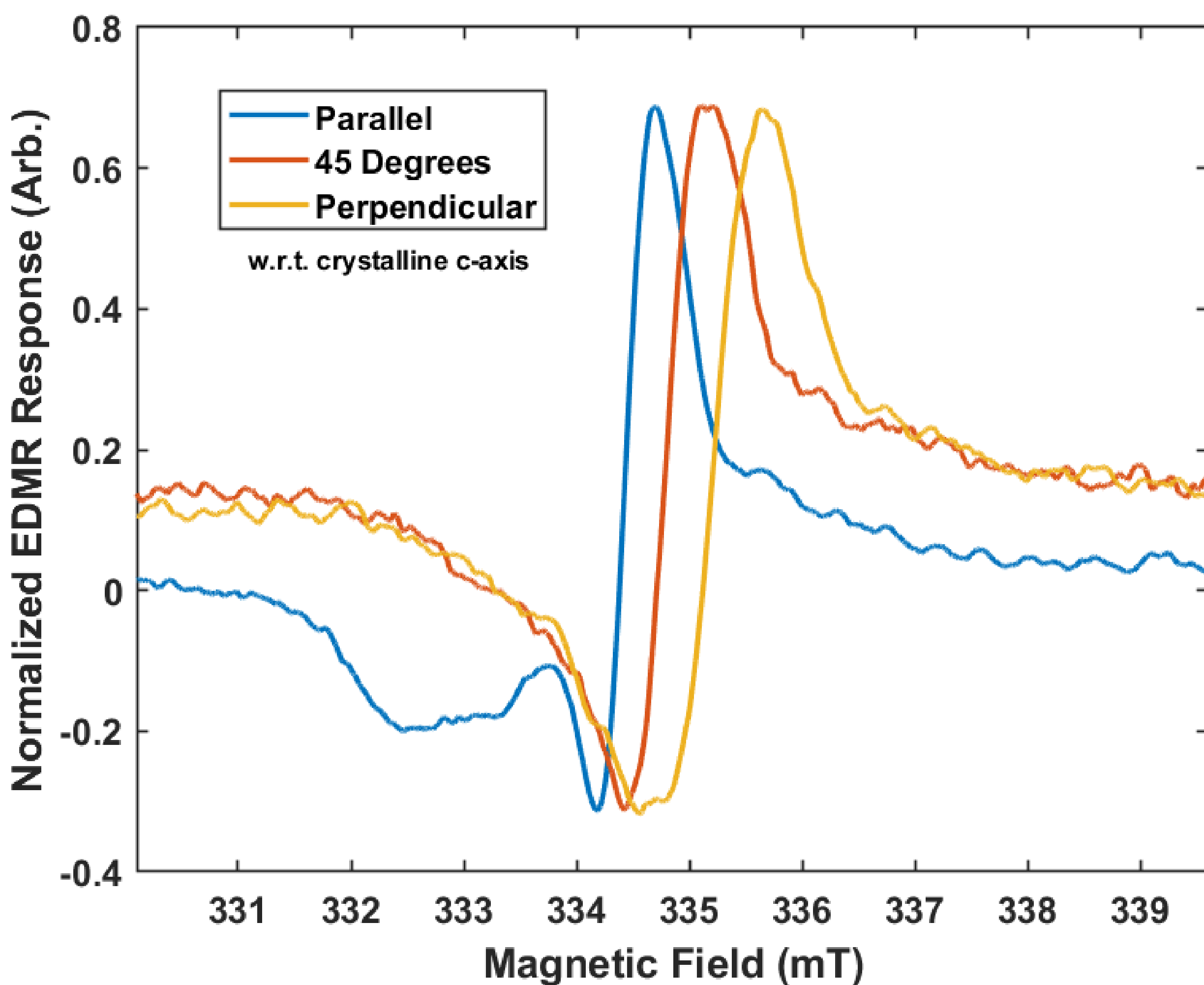

Figure 3-3: Rotation of the pin diode in B_0 from parallel to perpendicular orientation. The shape and width of the response changes appreciably. The width of the perpendicular response is ~0.5 mT wider than that of the parallel response.

This is accompanied by a significant broadening of the entire response's linewidth as a function of forward bias that is absent in the parallel response. Both signals increase in amplitude as a function of forward bias. However, from tracking the SDR amplitude of the V_{Si}^{-} response's

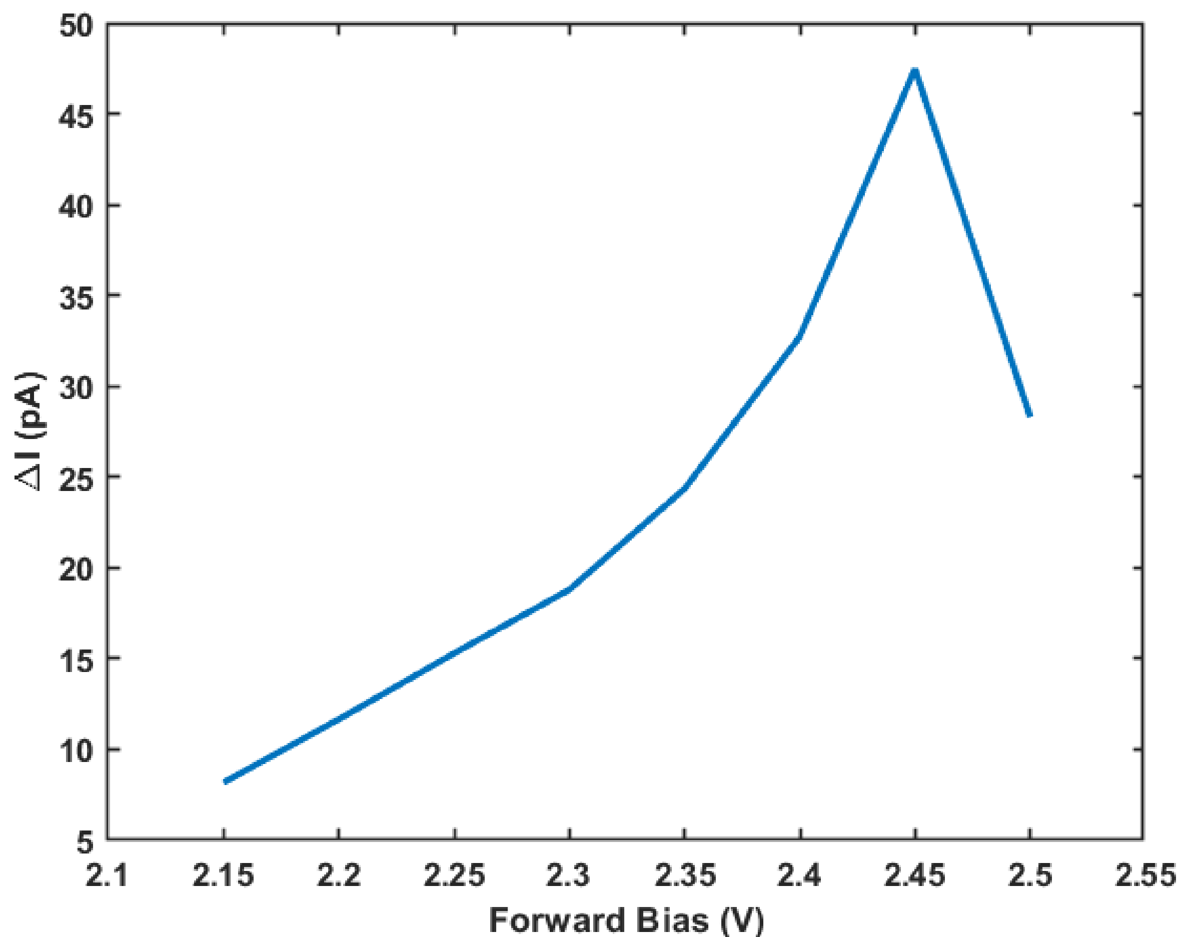

Figure 3-4: The change in EDMR amplitude as a function of forward bias.

integrated intensity as a function of forward bias, it is apparent that it saturates around the forward bias that the AF1 appears (Fig 3-4).

Going to higher forward bias magnitudes results in the shape of the spectrum being dominated more evenly by both signals (Fig 3-5).

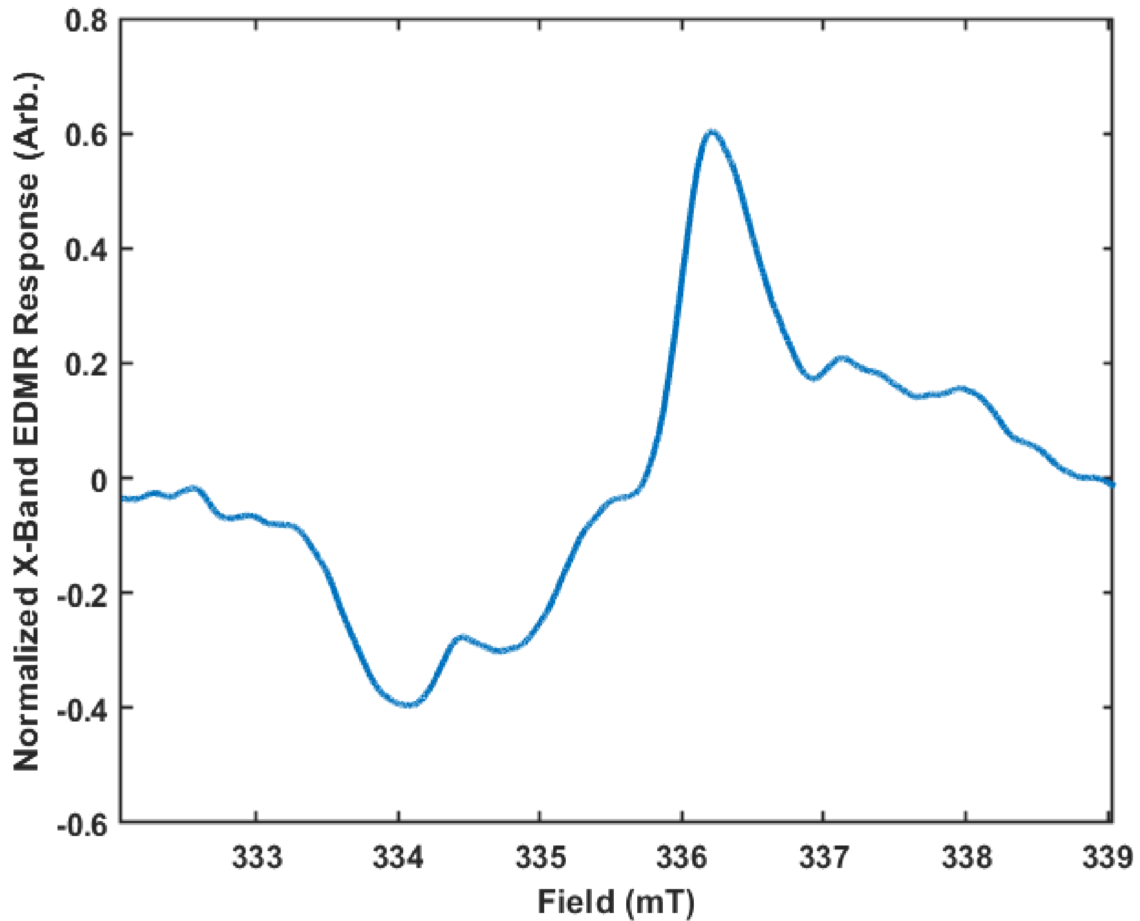

Figure 3-5: EDMR response of pin diode with 2.6 V applied forward bias oriented parallel to B_0. The spectrum is nearly evenly dominated by the AF1 and V_{Si}^-.

It was not possible to collect EDMR data beyond a forward bias magnitude of 2.65V due to issues with the signal-to-noise (SNR) ratio. SNR deteriorated with increasing forward bias due to unstable device current possibly stemming from a heat-current feedback loop. A significant amount of current flows through the diodes at high forward bias causing them to heat up. Increasing temperature results in an increase in the intrinsic carrier concentration, thus an increase in device current. Due to this, I am unsure at which forward bias the AF1 signal saturates.

The X-band EDMR response of the p-well diodes are markedly different than those of the pin diode. At low forward bias, it is apparent that the spectrum consists of more than just the V_{Si}^{-} as can be seen in (Fig 3-6).

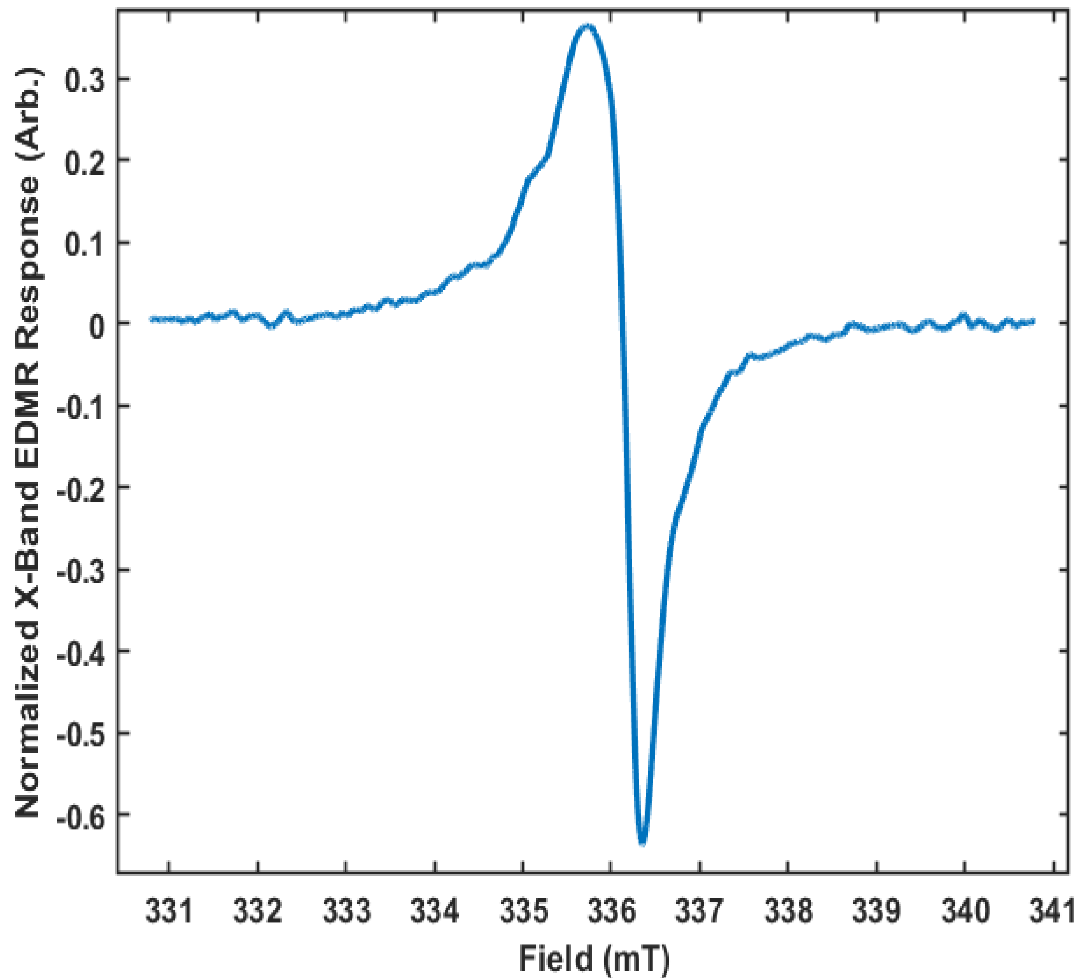

Figure 3-6: EDMR response of p-well diode forward biased at 2.20 V with the c-axis parallel to B_0.

There is a noticeable asymmetry in the line shape with the left side of the response having a breadth that is not reflected in the right side. Another point of departure in the p-well response is anisotropy in the g-values. Nearly consistent across the range of forward biases, $g_{\|} = 2.0035 \pm 0.003$ and $g_{\perp} = 2.0029 \pm 0.003$. An interesting, yet so far unexplainable, observation is that the

low bias (2.20V) responses had inverse g-values ($g_{\parallel} = 2.0029$ and $g_{\perp} = 2.0035$). There exists a signal in the p-well response that is located at and grows in amplitude similarly to the AF1 signal observed in the pin diodes (Fig. 3-6 to 3-8).

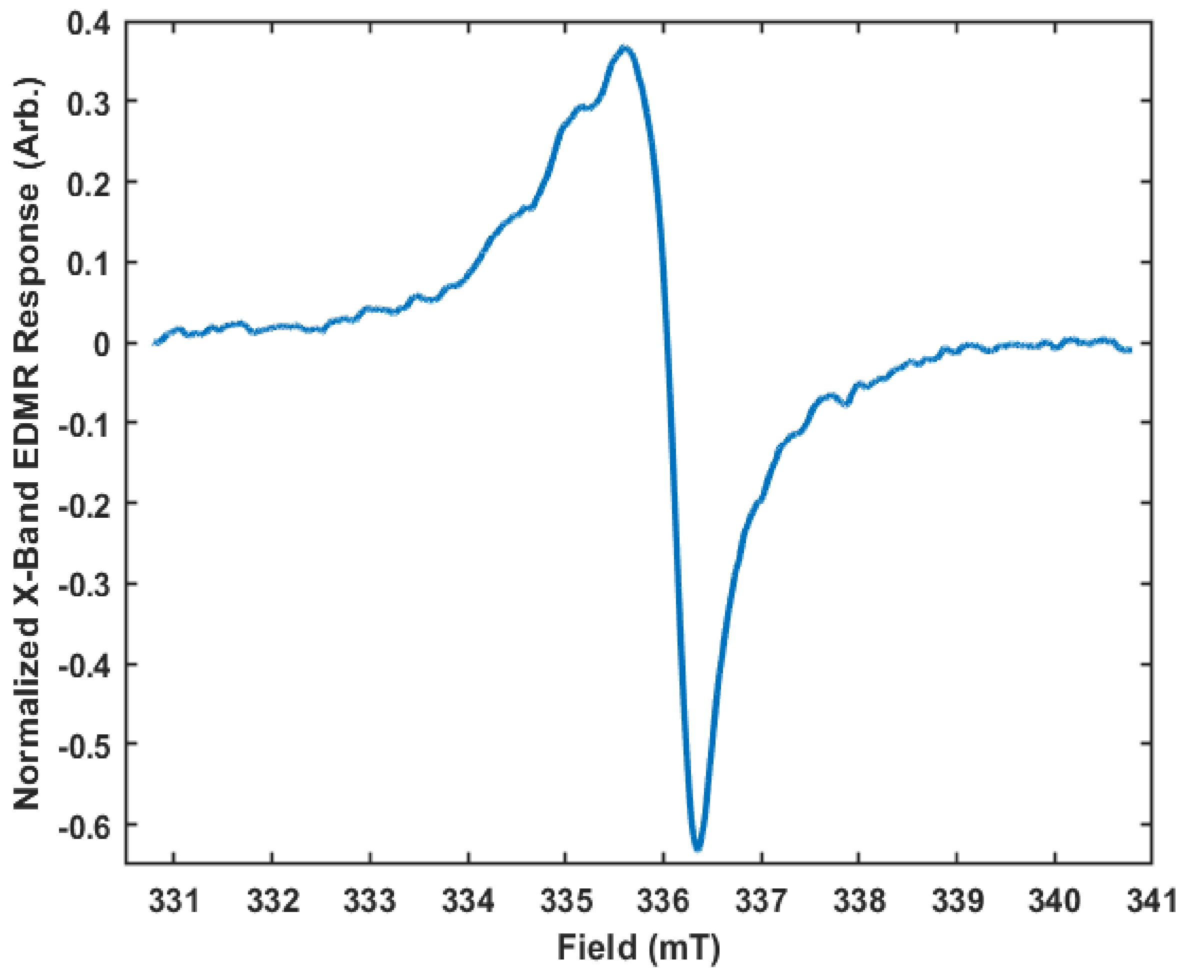

Figure 3-7: EDMR response of p-well diode forward biased at 2.40 V with the c-axis parallel to B_0.

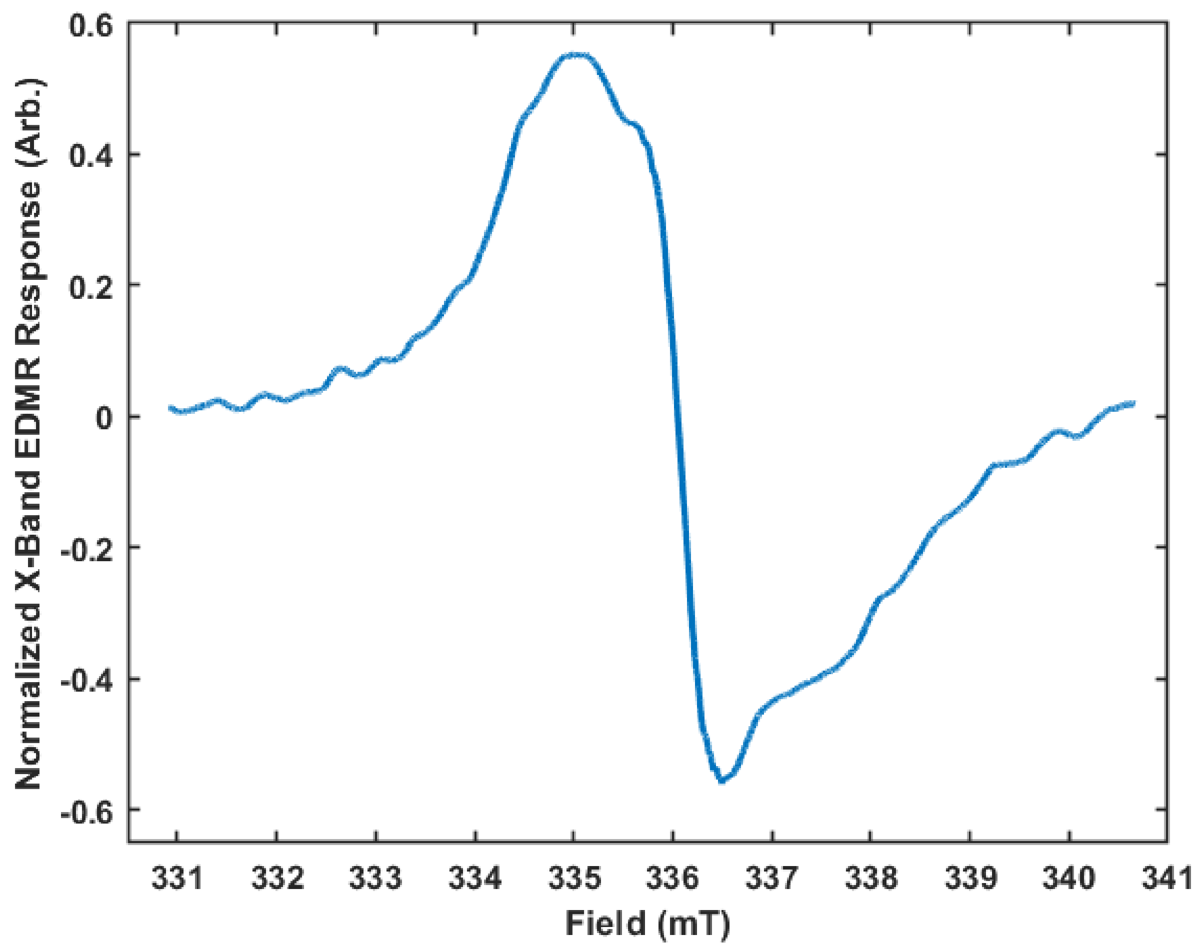

Figure 3-8: EDMR response of p-well diode forward biased at 2.60 V with the c-axis parallel to B_0.

Chapter 4

Discussion

This thesis presents the first exploration into the paramagnetic defect centers of 4H-SiC pin diodes via EDMR. Numerous features of the recorded spectra change as a function of forward bias including the amplitude, width, and line shape. When an SDR response is caused by a single type of defect (just V_{Si} for instance), only the amplitude of the response is expected to change with forward bias. The complicated structure of the diode response most likely indicates contributions from multiple defects. At low forward bias the pin diodes exhibit an isotropic SDR response with a g of 2.0030±0.0003 which is most likely due to the V_{Si}^-. Without detailed HF analysis it is impossible to determine if this response is primarily from the *h* or *k* site. The p-well device has a slightly more anisotropic *g* ranging between 2.0025-2.0035. An odd phenomenon that I have not observed anywhere else in the literature is that the lowest bias data points have inverse *g* values from the higher bias data. More specifically, at $V_F = 2.20$, $g_\perp = 2.0036 \pm 0.0003$ and $g_\parallel = 2.0029 \pm 0.0003$. At biases above $V_F = 2.20$, the average values are $g_\perp = 2.0027 \pm 0.0003$ and $g_\parallel = 2.0035 \pm 0.0003$. Currently I do not have a sound explanation for what causes this and can only hazard a guess that a different defect dominates the low bias SDR response with very similar but inverse g values as the defect which dominates the high bias SDR response. As forward bias is increased, a new signal is observed in both devices at a higher *g* (lower field) in conjunction with the V_{Si}^-. It should be noted that while the spectra for both devices seem to be heavily influenced by the V_{Si}^- and this other high-bias defect, there are many nuanced differences in their line shapes that are not easily described yet make it clear that different spin-dependent processes are taking place in each device. One possible cause could be the differences in the doping of the devices. The pin is n-epi ($N_d = 8 \times 15$ cm^{-3}) and the P-well is P-type ($N_a = 1 \times 17$ cm^{-3}). Doping of the intrinsic region for each device is also carried out

differently. The N-epi incorporates nitrogen into the 4H-SiC crystal as it is growing by controlling the C/Si ratio during CVD while the p-well is accomplished by bombarding the N-epi with aluminum ions. Ion bombardment is carried out at extremely high energies (~MeV) and is a very violent process at the atomic scale that creates many intrinsic defects. However, even the gentler doping method used to create the N-epi leads to high concentrations of intrinsic defects by virtue of the impurity atoms disturbing the perfect order of the crystal. These defects decrease the lifetime of injected minority carriers by increasing the concentration of recombination centers. Tawara et al studied minority carrier lifetime in N-epi 4H-SiC pin diodes [60]. They found that increasing the donor concentration of the N-epi significantly decreased the minority carrier lifetime of injected carriers. Through studying the minority carrier lifetime, they were able to determine which of the three bulk recombination methods were dominant at different doping and injected carrier concentrations. They found that for low-doped N-epi ($N_d < 8 \times 17$ cm^{-3}) at room temperature that SRH recombination significantly dominates both Auger and band-to-band recombination. Additionally, they determined that minority carrier lifetime dropped off with increasing minority carrier injection. Consequently, there is an inverse relationship between minority carrier lifetime and forward bias as carrier injection increases with increasing forward bias. Minority carrier injection increases with increasing forward bias. This decrease in the lifetime correlates to a decrease in the diffusion length of the charge carriers. A result of this is that the charge carriers are passing through a smaller segment of the intrinsic region before recombination. Therefore, they may not encounter defects that are more heavily localized to parts of the intrinsic region outside of the diffusion length. Conversely, they more heavily interact with defects localized to the region they are primarily passing through and with an increase in the carrier concentration the SDR signal from those defects would increase. It is not hard to imagine that these differences would cause a difference is the SDR response.

A possible explanation for why we begin to observe new SDR signals beyond a threshold forward bias comes from Grove and Fitzgerald. In their 1966 paper, "Surface effects on p-n junctions: Characteristics of surface space-charge regions under non-equilibrium conditions" they state that the range of the bandgap explored is equal to $qV_f/2$ centered around the middle of the bandgap, where V_f is forward bias and q is the charge of an electron. Their derivation is neither material nor device specific, hence it should provide insight here [59]. As the range of the bandgap explored increases, defects with energy levels further away from midgap can begin to populate and contribute to the SDR response as paramagnetic centers. If what Grove and Fitzgerald postulate holds true, it would add the ability to determine defect energy levels to EDMR. So far this is primarily established by DLTS which has yet to be confirmed with EPR/EDMR. (An alternate explanation could be band bending bringing the electron quasi-Fermi level above the defect energy level allowing it to populate.)

Aside from V_{Si}^- in the bulk, there are some other notable types of defects that could be present from different processing steps such as N_C, V_{Si} altered by N, and P_{bC}. First I will discuss the interfacial defects followed by the N related defects.

The defects suspected to be dominant near the 4H-SiC/SiO_2 interface are the negatively charged silicon vacancy and the carbon dangling bond (P_{bC}). It is not clear if the quasi cubic or hexagonal site of V_{Si}^- are equally abundant or not near the interface. The P_{bC} is a carbon dangling bond at the 4H-SiC/SiO2 interface which in some devices is believed to have a density of $3-4\times10^{12}$ cm^{-2} [61]. PbC are thought to form during oxidation from strain relaxation effects due to the lattice parameter mismatch of 4H-SiC and SiO_2 [61]. When SiO_2 forms, O_2 molecules diffuse to the 4H-SiC surface and adsorb, making bonds initially with the Si or C adatoms on that face forming solid SiO_2 and gaseous CO. As the oxide grows, more O_2 diffuses through the oxide to the interface effectively eating into the 4H-SiC. Gruber et al believe axial C bonds are less likely

to break because they point down into the bulk as opposed to the basal bonds that are more in line with the interfacial plane [62]. However, Umeda et al argued that the dangling bonds in their samples result from axial bonds on the (0001) face from comparison of HF data to models. There is some discrepancy in the reported g-values of the P_{bC}. In 2004, Cantin et al reported $g_{\parallel} = 2.0023$ and $g_{\perp} = 2.0032$, while in 2020 Umeda et al reported $g_{\parallel} = 2.0029$ and $g_{\perp} = 2.0032$ [63,61]. Theoretically, the values should be the same regardless of detection scheme, however I am inclined to trust the much more sensitive EDMR measurement conducted by Umeda et al. Factoring in the linewidth of the signals and experimental error, the P_{bC} and V_{Si}^{-} SDR responses overlap somewhat. Both pin and p-well diodes have a 4H-SiC/SiO_2 interface in the electrically active regions where most of the spin dependent recombination is taking place, thus there is a high likelihood of P_{bC} centers contributing to the SDR response of both diodes. The P_{bC} is accompanied by two sets of HF lines from C^{13} and Si^{29} with a splitting of 161-237 G ($A_{\parallel}$ and A_T, respectively) and 66 G, respectively. Relative intensities of the C^{13} and Si^{29} are 1.1% and 12.7%, respectively [61]. Unfortunately, I was not able to definitively resolve these HF signals in my spectra.

Nitrogen is the donor dopant of choice for n-type 4H-SiC. It is incorporated substitutionally in the lattice during epitaxial growth from the gaseous environment and via the much more violent ion implantation process. Both methods create point defects in the 4H-SiC lattice by displacing the C for which N substitutes (N_C). Due to there being two inequivalent lattice sites in 4H-SiC there are two inequivalent N_C defects; one for the quasi-cubic, N_C(k), and one for the hexagonal site, N_C(h). Both sites have anisotropic *g*-values; N_C(h): $g_{\parallel}$=2.0055, g_{T}=2.0010 and N_C(k): $g_{\parallel}$=2.0043, g_T=2.0013 [64]. N^{14} is 99.6% abundant with a nuclear spin $I = 1$. This gives rise to three additional lines due to HF interactions. Additionally, N_C forms a complex defect with V_{Si} ($N_C V_{Si}$) which, at least theoretically, broadens the EDMR response of V_{Si} [65]. N tends to incorporate at the 25 third-nearest neighbor C sites [65]. This broadening is due to the HF

interactions and possibly the increased lattice disorder introduced by N_C [64,66]. The high *g*-value of the N_C SDR response when the field is parallel to the crystalline c-axis of 4H-SiC fits within the possible range of *g* that could be attributed to the AF1/2 signal. It is difficult to attribute a center crossing to the AF1/2 signal, but it is most likely within the range of 2.0040-2.0065 depending on the attributed intensity and linewidth. However, if the AF1/2 were due to $N_C(h/k)$ I might expect a similar signal to appear on the high-field side of the dominant SDR signal when the device is rotated so that the c-axis is perpendicular to **B** as the dominant SDR signal of my spectrum is isotropic. However, because the **B⊥c** response of N_C is much closer in *g* to the dominating isotropic response, a separate feature would not be expected as much as a broadening of the dominating response due to a partial overlap of the SDR responses. At the hexagonal site, N_C exhibits a negligible hyperfine splitting of ~1G, however, at the quasi-cubic site there is a more appreciable splitting of ~ 18G [64]. Szasz et al found the intensity ratio of the HF response to be 5% that of the main signal in 6H-SiC [67]. Assuming the intensity ratio would be similar in 4H-SiC, it makes sense that we are not able to properly resolve these HF signals and cannot perform a definitive identification of N_C in our samples. An opportunity to perform terahertz EDMR on our devices would allow us to separate the HF from the main signal and possibly achieve this identification.

There is good reason to suspect paramagnetic N_C centers are present in the GE diodes as N is used to dope the N+ and n-epi diode regions. Additionally, the relatively isotropic *g* of the dominant spectral line is indicative of V_{Si}. However, the dominant spectral feature of my data has a width of about 5-6 G, whereas it is supposed to be closer to 3 G. Ashton et al saw the SDR response of V_{Si} broaden from 4 g to 10 G after NO anneal in MOSFETs [66]. Although I do not observe the same amount of broadening, HF interactions with V_{Si} from third-nearest neighbor N could explain the width of my signals. In the future, conducting ultra-high frequency (240 Terahertz) EDMR would theoretically allow for us to separate the HF signal from the dominant

SDR response. By then performing this ultra-high frequency in at least two perpendicular orientations we could determine the map of the HF *g*-values to positively identify if magnetic N_C is influencing the V_{Si} SDR response.

Future work would greatly aid in the identification of the AF1/2 center. One of the main hinderances is my inability to attribute a definitive identification of the signals in my spectra is SNR and overlapping SDR signals obscuring HF signals. Two ways that other groups have isolated HF interactions is by performing multi-frequency and low temperature EDMR. Performing EDMR at 240 GHz would allow us to separate the signals and more positively attribute a g-value to AF1/2. Performing EDMR at temperatures much lower than room temperature would increase the SNR and allow us to take data at higher forward biases. Access to an apparatus which would allow us to observe the response along the z-axis would determine if the defect has axial or rhombic symmetry and allow us to compare our results more accurately to those existing in the literature. Additionally, by bonding the diodes between the surface P+ and back (substrate) N+ contacts and performing identical EDMR experiments we could compare results to rule out the effects of the interfacial region.

Chapter 5

Conclusion

In conclusion, EDMR was performed on two different types of diodes fabricated by General Electric Research in an attempt to identify the paramagnetic point defects in the electrically active regions of the diodes that could impact their performance. I was able to reasonably conclude that the singly negative charged silicon vacancy, V^{-}_{Si}, is present in at least the pin diode but most likely the p-well diode as well. Additionally, I believe the V^{-}_{C} defect to also be present due to the statistical likelihood, however I was unable to prove this hypothesis. However, another carbon related defect, the P_{bC}, seems to be a good fit for the data and is reasonable to expect from the presence of a 4H-SiC/SiO_2 interface so close to the electrically active regions where a majority of recombination is occurring. Due to the linewidths of my signals being slightly wider than theory and past EPR/EDMR predict, I am also under the assumption that N_C is present in the diodes. Unfortunately, I was unable to resolve HF data. This work should serve as a strong start point for further exploration into the paramagnetic defect centers present in these diodes.

References

1. A. Huang, "Power Semiconductor Devices for Smart Grid and Renewable Energy Systems", *Proceedings of the IEEE*, vol. 105, no. 11, pp. 2019-2047, 2017. Available: 10.1109/jproc.2017.2687701.
2. T. Umeda, J. Isoya, N. Morishita, T. Ohshima and T. Kamiya, "EPR identification of two types of carbon vacancies in 4H-SiC", *Physical Review B*, vol. 69, no. 12, 2004. Available: 10.1103/physrevb.69.121201.
3. B. Van Zeghbroeck, *Principles of semiconductor devices and heterojunctions*. Upper Saddle River, N.J.: Prentice Hall, 2010.
4. B. Doherty, *PIN Diode Fundamentals*. Watertown: Microsemi.
5. G. Vacca, "Benefits and advantages of silicon carbide power devices over their silicon counterparts", *Semiconductor-today.com*, 2017. [Online]. Available: http://www.semiconductor-today.com/features/PDF/semiconductor-today-apr-may-2017-Benefits-and-advantages.pdf.
6. J. Taillon, "Characterization of 4H-SiC MOSFETs | Joshua Taillon", *Joshua Taillon*, 2022. [Online]. Available: https://www.joshuataillon.com/project/silicon-carbide/.
7. W. Doherty, "A COMPARISON OF PIN DIODE & RECTIFIER DIODE CHARACTEISTICS", *Microsemi.com*, 1998. [Online]. Available: https://www.microsemi.com/sites/default/files/datasheets/Products/rf/APPENDIX%20B.pdf.
8. T. Ayalew, "SiC Semiconductor Devices Technology, Modeling, and Simulation", Ph.D, TU Wien, 2004.

9. V. Krasnov, S. Shutov, S. Yerochin and O. Demenskyi, "High Temperature Operation Limit Assessment for 4H-SiC Schottky Diode-Based Extreme Temperature Sensors", *IEEE Sensors Journal*, vol. 19, no. 5, pp. 1640-1644, 2019. Available: 10.1109/jsen.2018.2883544.
10. X. Guo, Q. Xun, Z. Li and S. Du, "Silicon Carbide Converters and MEMS Devices for High-temperature Power Electronics: A Critical Review", *Micromachines*, vol. 10, no. 6, p. 406, 2019. Available: 10.3390/mi10060406 [Accessed 29 May 2022].
11. S. Kargarrazi, H. Elahipanah, S. Rodriguez and C. Zetterling, "500 °C, High Current Linear Voltage Regulator in 4H-SiC BJT Technology", *IEEE Electron Device Letters*, vol. 39, no. 4, pp. 548-551, 2018. Available: 10.1109/led.2018.2805229 [Accessed 29 May 2022].
12. K. Tian et al., "Comprehensive Characterization of the 4H-SiC Planar and Trench Gate MOSFETs From Cryogenic to High Temperature", *IEEE Transactions on Electron Devices*, vol. 66, no. 10, pp. 4279-4286, 2019. Available: 10.1109/ted.2019.2934507 [Accessed 29 May 2022].
13. R. Gao et al., "Radiation tolerance analysis of 4H-SiC PIN diode detectors for neutron irradiation", *Sensors and Actuators A: Physical*, vol. 333, p. 113241, 2022. Available: 10.1016/j.sna.2021.113241 [Accessed 29 May 2022].
14. G. Harris, *Properties of silicon carbide*. London: INSPEC, 1995.
15. "Electrical properties of Silicon (Si)", *Ioffe.ru*. [Online]. Available: http://www.ioffe.ru/SVA/NSM/Semicond/Si/electric.html. [Accessed: 29- May- 2022].
16. K. Sheng, Y. Zhang, L. Yu, M. Su and J. Zhao, "High-Frequency Switching of SiC High-Voltage LJFET", *IEEE Transactions on Power Electronics*, vol. 24, no. 1, pp. 271-277, 2009. Available: 10.1109/tpel.2008.2005984 [Accessed 29 May 2022].

17. Singh, R., Baliga, B.J. (1998). P-I-N Diode. In: Cryogenic Operation of Silicon Power Devices. The Springer International Series in Engineering and Computer Science. Springer, Boston, MA. https://doi.org/10.1007/978-1-4615-5751-7_4
18. "PIN DIODE PHYSICS", *Microsemi.com*, 1998. [Online]. Available: https://www.microsemi.com/sites/default/files/datasheets/Products/rf/APPENDIX%20A.pdf. [Accessed: 29- May- 2022].
19. Lutz, J., Schlangenotto, H., Scheuermann, U., De Doncker, R. (2018). pin Diodes. In: Semiconductor Power Devices. Springer, Cham. https://doi.org/10.1007/978-3-319-70917-8_5
20. "Dirac equation - Wikipedia", *En.wikipedia.org*, 2022. [Online]. Available: https://en.wikipedia.org/wiki/Dirac_equation#Solutions. [Accessed: 30- May- 2022].
21. W. Gordy, *Theory and applications of electron spin resonance*. New York: Wiley, 1980.
22. J. Weil and J. Bolton, *Electron paramagnetic resonance*. Hoboken: Wiley-Interscience, 2007.
23. "Zeeman", *Epr.ethz.ch*, 2022. [Online]. Available: https://epr.ethz.ch/education/basic-concepts-of-epr/one-elect--in-the-magn--field/zeeman.html. [Accessed: 30- May- 2022].
24. J. Klare, "Site-directed spin labeling EPR spectroscopy in protein research", *bchm*, vol. 394, no. 10, pp. 1281-1300, 2013. Available: 10.1515/hsz-2013-0155 [Accessed 30 May 2022].
25. C. J. Cochrane, "Development of New Atomic Scale Defect Identification Schemes in Micro/Nanoelectronics Incorporating Digital Signal Processing Methods for Investigating Zero/Low Field Spin Dependent Transport and Passage Effects in Electrically Detected Magnetic Resonance," Penn State, 2013.
26. J. Huang, H. Kuo and S. Shen, *Nitride semiconductor light-emitting diodes (LEDs)*. Woodhead Publishing Limited, 2014.

27. R. Hui and M. O'Sullivan, *FIBER OPTIC MEASUREMENT TECHNIQUES*. [S.l.]: ELSEVIER ACADEMIC PRESS, 2009.

28. R. Hall, "Electron-Hole Recombination in Germanium", *Physical Review*, vol. 87, no. 2, pp. 387-387, 1952. Available: 10.1103/physrev.87.387 [Accessed 30 May 2022].

29. W. Shockley and W. Read, "Statistics of the Recombinations of Holes and Electrons", *Physical Review*, vol. 87, no. 5, pp. 835-842, 1952. Available: 10.1103/physrev.87.835 [Accessed 30 May 2022].

30. P. Lenahan and M. Jupina, "Spin dependent recombination at the silicon/silicon dioxide interface", *Colloids and Surfaces*, vol. 45, pp. 191-211, 1990. Available: 10.1016/0166-6622(90)80023-w [Accessed 31 May 2022].

31. D. Kaplan, I. Solomon, and N. F. Mott, "Explanation of the large spin-dependent recombination effect in semiconductors," J. Phys. Letters, vol. 39, no. 4, pp. 51–54, 1978.

32. T. Hornos, A. Gali and B. Svensson, "Large-Scale Electronic Structure Calculations of Vacancies in 4H-SiC Using the Heyd-Scuseria-Ernzerhof Screened Hybrid Density Functional", *Materials Science Forum*, vol. 679-680, pp. 261-264, 2011. Available: 10.4028/www.scientific.net/msf.679-680.261 [Accessed 31 May 2022].

33. N. Mizuochi, S. Yamasaki, and T. Ohshima, "EPR studies of the isolated negatively charged silicon vacancies in n-type 4H-and 6H-SiC: Identification of C3v symmetry and silicon sites", *Phys. Rev. B- Condensed Matter and Materials Physics,* vol. 68, Iss. 16, 2003. Available: https://doi.org/10.1103/PhysRevB.68.165206

34. Y. Abe et al., "Electrical detection of Tv2a-type silicon vacancy spin defect in 4H-SiC MOSFETs", *Applied Physics Letters*, vol. 120, no. 6, p. 064001, 2022. Available: 10.1063/5.0078189 [Accessed 1 June 2022].

35. J. Ashton, S. Moxim, A. Purcell, P. Lenahan and J. Ryan, "A quantitative model for the bipolar amplification effect: A new method to determine semiconductor/oxide interface state densities", *Journal of Applied Physics*, vol. 130, no. 13, p. 134501, 2021. Available: 10.1063/5.0064397 [Accessed 1 June 2022].

36. T. Umeda et al., "EPR and theoretical studies of negatively charged carbon vacancy in 4H-SiC", *Physical Review B*, vol. 71, no. 19, 2005. Available: 10.1103/physrevb.71.193202 [Accessed 1 June 2022].

37. C. Cochrane, P. Lenahan and A. Lelis, "An electrically detected magnetic resonance study of performance limiting defects in SiC metal oxide semiconductor field effect transistors", *Journal of Applied Physics*, vol. 109, no. 1, p. 014506, 2011. Available: 10.1063/1.3530600 [Accessed 1 June 2022].

38. R.C. Glass, D. Henshall, V.F. Tsvetkov, and C.H. Carter, Jr., "SiC Seeded Crystal Growth," Physica Status Solidi (b), vol. 202, p. 149, 1997

39. Y. Gu, L. Shi, J. Luo, S. Li and L. Wang, "Directly Confirming the Z(1/2) Center as the Electron Trap in SiC Through Accessing the Nonradiative Recombination", *physica status solidi (RRL) – Rapid Research Letters*, vol. 16, no. 2, p. 2100458, 2021. Available: 10.1002/pssr.202100458 [Accessed 6 June 2022].

40. P. Klein et al., "Lifetime-limiting defects in n− 4H-SiC epilayers", *Applied Physics Letters*, vol. 88, no. 5, p. 052110, 2006. Available: 10.1063/1.2170144 [Accessed 6 June 2022].

41. N. Son et al., "Negative-U System of Carbon Vacancy in 4H-SiC", 2012.

42. C. Hemmingsson, N. Son, A. Ellison, J. Zhang and E. Janzén, "Negative-U centers in 4H silicon carbide", *Physical Review B*, vol. 58, no. 16, pp. R10119-R10122, 1998. Available: 10.1103/physrevb.58.r10119 [Accessed 6 June 2022].

43. X. Trinh et al., "Negative-U carbon vacancy in 4H-SiC: Assessment of charge correction schemes and identification of the negative carbon vacancy at the quasicubic site", *Physical Review B*, vol. 88, no. 23, 2013. Available: 10.1103/physrevb.88.235209 [Accessed 6 June 2022].

44. L. Storasta and H. Tsuchida, "Reduction of traps and improvement of carrier lifetime in 4H-SiC epilayers by ion implantation", *Applied Physics Letters*, vol. 90, no. 6, p. 062116, 2007. Available: 10.1063/1.2472530 [Accessed 6 June 2022].

45. H. Ayedh, R. Nipoti, A. Hallén and B. Svensson, "Thermodynamic equilibration of the carbon vacancy in 4H-SiC: A lifetime limiting defect", *Journal of Applied Physics*, vol. 122, no. 2, p. 025701, 2017. Available: 10.1063/1.4991815 [Accessed 6 June 2022].T.

46. T. Kimoto and Y. Yonezawa, "Current status and perspectives of ultrahigh-voltage SiC power devices", *Materials Science in Semiconductor Processing*, vol. 78, pp. 43-56, 2018. Available: 10.1016/j.mssp.2017.10.010 [Accessed 24 June 2022].

47. M. Hori and Y. Ono, "Charge Pumping Under Spin Resonance in Si(100) Metal-Oxide-Semiconductor Transistors", 2022. .

48. M. Anders, P. Lenahan and A. Lelis, "Multi-resonance frequency spin dependent charge pumping and spin dependent recombination - applied to the 4H-SiC/SiO2 interface", *Journal of Applied Physics*, vol. 122, no. 23, p. 234503, 2017. Available: 10.1063/1.4996298.

49. G. Hahn and S. Joos, "State-of-the-Art Industrial Crystalline Silicon Solar Cells", Advances in Photovoltaics: Part 3, pp. 1-72, 2014. Available: 10.1016/b978-0-12-388417-6.00005-2.

50. L. Torpo, M. Marlo, T. Staab and R. Nieminen, "Comprehensive ab initio study of properties of monovacancies and antisites in 4H-SiC", *Journal of Physics: Condensed Matter*, vol. 13, no. 28, pp. 6203-6231, 2001. Available: 10.1088/0953-8984/13/28/305

51. X. Yan, P. Li, L. Kang, S. Wei and B. Huang, "First-principles study of electronic and diffusion properties of intrinsic defects in 4H-SiC", Journal of Applied Physics, vol. 127, no. 8, p. 085702, 2020. Available: 10.1063/1.5140692.

52. T. Kobayashi, K. Harada, Y. Kumagai, F. Oba and Y. Matsushita, "Native point defects and carbon clusters in 4H-SiC: A hybrid functional study", Journal of Applied Physics, vol. 125, no. 12, p. 125701, 2019. Available: 10.1063/1.5089174.

53. S. Orlinski, J. Schmidt, E. Mokhov and P. Baranov, "Silicon and carbon vacancies in neutron-irradiated SiC: A high-field electron paramagnetic resonance study", Physical Review B, vol. 67, no. 12, 2003. Available: 10.1103/physrevb.67.125207.

54. T. Wimbauer, B. Meyer, A. Hofstaetter, A. Scharmann and H. Overhof, "Negatively charged Si vacancy in4HSiC: A comparison between theory and experiment", Physical Review B, vol. 56, no. 12, pp. 7384-7388, 1997. Available: 10.1103/physrevb.56.7384.

55. N. Mizuochi et al., "Continuous-wave and pulsed EPR study of the negatively charged silicon vacancy withS=32andC3vsymmetry inn-type4H−SiC", Physical Review B, vol. 66, no. 23, 2002. Available: 10.1103/physrevb.66.235202.

56. E. Janzen, A. Gali, A. Henry, I. G. Irancv, B. Magnusson, and N. Son, “Defects in Microelectronic Materials and Devices”, edited by D. M. Fleetwood, S. T. Panlelides, and R. D. Schrimpf CRC, Boca Raton, 2009, Chap. 21.

57. M. MacMillan, "Silicon Carbide Epitaxy For Beginners", *Poweramericainstitute.org*, 2021. [Online].

58. D. Larkin, "SiC Dopant Incorporation Control Using Site-Competition CVD", *physica status solidi (b)*, vol. 202, no. 1, pp. 305-320, 1997. Available: 10.1002/1521-3951(199707)202:1<305::aid-pssb305>3.0.co;2-9.

59. A. Grove and D. Fitzgerald, "Surface effects on p-n junctions: Characteristics of surface space-charge regions under non-equilibrium conditions", *Solid-State Electronics*, vol. 9, no. 8, pp. 783-806, 1966. Available: 10.1016/0038-1101(66)90118-3.

60. Tawara, T. et al. (2016) “Short minority carrier lifetimes in highly nitrogen-doped 4H-sic epilayers for suppression of the stacking fault formation in PIN diodes,” Journal of Applied Physics, 120(11), p. 115101. Available at: https://doi.org/10.1063/1.4962717.

61. Umeda, T. et al. (2020) “Carbon dangling-bond center (carbon pb center) at 4H-sic(0001)/sio2 interface,” Applied Physics Letters, 116(7), p. 071604. Available at: https://doi.org/10.1063/1.5143555.

62. Gruber, G. et al. (2018) “Electrically detected magnetic resonance of carbon dangling bonds at the Si-Face 4H-sic/SIO2 interface,” Journal of Applied Physics, 123(16), p. 161514. Available at: https://doi.org/10.1063/1.4985856.

63. Cantin, J.L. et al. (2004) “Identification of the carbon dangling bond center at the 4H-SiC/SiO2 interface by an EPR study in oxidized porous SiC,” Physical Review Letters, 92(1). Available at: https://doi.org/10.1103/physrevlett.92.015502.

64. Schubert, M. et al. (2022) “Terahertz electron paramagnetic resonance generalized spectroscopic ellipsometry: The magnetic response of the nitrogen defect in 4H-sic,” Applied Physics Letters, 120(10), p. 102101. Available at: https://doi.org/10.1063/5.0082353.

65. Anders, M.A., Lenahan, P.M. and Lelis, A.J. (2017) “Multi-resonance frequency spin dependent charge pumping and spin dependent recombination - applied to the 4H-SiC/SiO2 interface,” Journal of Applied Physics, 122(23), p. 234503. Available at: https://doi.org/10.1063/1.4996298.
66. Ashton, J.P. et al. (2019) “Electrically detected magnetic resonance study of barium and nitric oxide treatments of 4H-sic metal-oxide-semiconductor field-effect transistors,” Journal of Applied Physics, 126(14), p. 145702. Available at: https://doi.org/10.1063/1.5120704.
67. Szász, K. et al. (2014) “Theoretical and electron paramagnetic resonance studies of hyperfine interaction in nitrogen doped 4H and 6H-SiC,” Journal of Applied Physics, 115(7), p. 073705. Available at: https://doi.org/10.1063/1.4866331.
68. Pin diode (2022) Wikipedia. Wikimedia Foundation. Available at: https://en.wikipedia.org/wiki/PIN_diode.
69. PIN diode - working, characteristics, definition, applications (2022) BYJUS. BYJU'S. Available at: https://byjus.com/physics/pin-diode/.
70. Sharov, F. (16801) Applications of Electrically Detected Magnetic Resonance to the Analysis of Technologically Relevant Reliability Mechanisms in Semiconductor Devices. dissertation. Penn State